Chapter 2
Non-thermal X-Ray Enhancement Around Dense Gas Clumps

Supernova remnants (SNRs) have a profound influence on the interstellar medium (ISM) via shock interaction and injection of heavy elements. If the ISM is dense enough, this dynamical interaction can also affect the evolution of an SNR through the distortion of its shell morphology. It is therefore important to study the detailed physical properties of the interaction between SNRs and ISM to understand what can occur.

RX J1713.7−3946 is a unique SNR emitting very high energy (VHE, Energies $E > 100$ GeV) γ-rays and X-rays, which are likely emitted by cosmic ray particles accelerated in the SNR via diffusive shock acceleration (DSA; see Sect. 1.3.2 for details). Note that the X-rays of the SNR are purely non-thermal synchrotron emissions, indicating that cosmic ray electrons are accelerated in the SNR up to the 10 TeV range; in addition to RX J1713.7−3946, only two known SNRs produce such non-thermal X-rays: RX J0852.0−4622 (Vela Jr.) and HESS J1731−347 (e.g., Koyama et al. 1997; Slane et al. 2001; Tian et al. 2010). Detailed theoretical modeling of this high-energy radiation made over a wide range of physical parameters appropriate for the SNR has shown that the observed properties of high energy radiation can be reproduced under reasonable sets of physical parameters relevant to cosmic ray acceleration (e.g., Zirakashvili and Aharonian 2007, 2010). It is thus becoming increasingly important to observationally constrain the physical parameters of the SNR (such as its magnetic field) and their distributions.

As mentioned in Sect. 1.5.2, molecular clumps interacting with SNR RX J1 713.7−3946 were discovered in the ^{12}CO($J = 1$–0) emission at $V_{\rm LSR}$, the rest velocity with respect to the local reference frame (around -7 km s^{-1}). This shows that the distribution of the CO emission in RX J1713.7−3946 correlates well with the X-ray distribution in pc scale (Fukui et al. 2003, see Fig. 1.9 in Sect. 1.5.2); the northwestern rim of the X-ray image coincides with the most prominent CO peaks (Fukui et al. 2003; Moriguchi et al. 2005; Fukui 2008). This X-ray distribution is now theoretically interpreted as being caused by interaction between the shock front and the molecular clumps, as modeled in the magnetohydrodynamic (MHD) numerical simulations

H. Sano, *Shock-Cloud Interaction in RX J1713.7–3946*,
Springer Theses, DOI 10.1007/978-4-431-55636-7_2

by Inoue et al. (2009, 2012). This correlation provides a robust verification of the physical association of the CO clumps with the non-thermal X-ray shell. **However, to date, there has not been a quantitative study to clarify the connection among the X-rays, ISM clumps, and accelerated cosmic ray electrons.**

Furthermore, Fukui et al. (2003) found that CO peak C shows broad CO wings and suggested that these may result from dynamical acceleration by the SNR blast wave. Such broad molecular wings are found in several SNRs, including IC443, W44, and W28. (e.g., Denoyer 1979; Wootten 1977, 1981). Moriguchi et al. (2005) showed that the ^{12}CO(J = 3–2) distribution in peak C shows a hint of bipolarity, which could possibly be associated with the presence of an infrared compact source with the spectrum of a protostar. This may indicate an alternative possibility that the broad wings are driven by the outflow from a protostar rather than a shock interaction. The question whether the SNR is accelerating molecular gas to high velocities in peak C is yet unanswered. It is therefore important to clarify whether the CO broad wings are caused by blast-wave acceleration or protostellar activity.

In this chapter, we establish a connection between synchrotron X-rays and the surrounding ISM distribution. The present work is aimed at better understanding the SNR shock-cloud interaction and thereby establishing the origin of the distribution of synchrotron X-rays in SNR RX J1713.7−3946. This study will be extended to the other SNRs with non-thermal features, allowing us to deepen our understanding of the role of the interaction between high energy radiation and cosmic ray acceleration in the ISM. In this work, we show a comparison of the spatial distribution among CO, HI, and X-rays over the entire SNR to clarify the relationship between the dense gas and the high-energy electrons. Furthermore, we reveal the molecular properties of the core of RX J1713.7−3946, the broad wings in peak C, and the other cloud cores nearby.

2.1 Datasets of CO, HI, and X-Rays

2.1.1 CO

We conducted ^{12}CO(J = 2–1, 4–3) and ^{13}CO(J = 2–1) observations using the NANTEN2 4-m sub-mm telescope belonging to Nagoya University, which is installed at Pampa La Bola (4865 m above the sea level) in northern Chile.

The ^{12}CO(J = 2–1) and ^{13}CO(J = 2–1) data at 230 GHz were gathered from August to November 2008. The telescope used a 4 K cooled double sideband (DSB) receiver as a front end and had a typical system temperature of ∼250 K in the single sideband (SSB), including the atmosphere toward zenith. The telescope has an angular resolution (full width at half maximum; FWHM) of 90″ at 230 GHz. We used an acoustic optical spectrometer with 2,048 channels, a bandwidth of 390 km s^{-1}, and resolution per channel of 0.38 km s^{-1}. Observations in ^{12}CO(J = 2–1) were conducted in on-the-fly (OTF) mode with an integration time of 1.0 or

2.0 s per grid, producing a Nyquist-sampled 30″ grid dataset. The telescope has a beam size of 90″ at 230 GHz. The ambient temperature load was employed for intensity calibration. The absolute intensity scale was estimated by observing the Ori KL object [$5^h35^m14\overset{s}{.}52$; $-5°22'28\overset{''}{.}2$ (J2000)] (Schneider et al. 1998) at the ^{12}CO(J = 2–1) line. The main beam efficiency, η_{mb}, was estimated to be 0.83. The rms noise fluctuations with 1.0 and 2.0 s integrations were better than 0.66 and 0.51 K per channel, respectively. The pointing accuracy was estimated to be better than ∼15″ through two-hourly observations of Jupiter. Images were smoothed by means of a Gaussian kernel with a FWHM of 60″. Observations in ^{13}CO, including peaks A, B, C, and D, were conducted in the OTF mode over an area of 22 arcmin^2 (Moriguchi et al. 2005) with an integration time of 2.0 s, producing a Nyquist-sampled 30″ grid dataset. The pointing accuracy for this task was also checked through two-hourly Jupiter observations and was found to be as accurate as ∼15″, and the rms noise fluctuations were better than 0.68 K per channel. The ambient temperature load was also employed for absolute intensity calibration, which was calibrated by observing Oph EW4 [$16^h26^m21\overset{s}{.}92$; $-24°25'40\overset{''}{.}4$ (J2000)] (Kulesa et al. 2005).

Observations in ^{12}CO(J = 4–3) were conducted from November to December 2007 over a 9 arcmin^2 region, including peak C and toward a point in peak A. The telescope has a beam size of 38″ at 460 GHz, as measured by observing Jupiter. A SIS receiver with an SSB temperature of 300 K including the atmosphere toward zenith was used as a front end. The typical rms noise fluctuations were 0.28 K per channel, and absolute intensity calibration was conducted as described by Pineda et al. (2008).

In addition, we used the ^{12}CO(J = 1–0) data at 115 GHz taken with the NANTEN 4-m telescope, as published in Moriguchi et al. (2005). The angular resolution of the data is 2.′6 (FWHM) and the velocity resolution and rms noise fluctuations are 0.65 km s^{-1} and 0.3 K, respectively. Observations were conducted in position-switching mode with a 2′ grid spacing (for more detailed information, see also Moriguchi et al. 2005). The ^{12}CO(J = 2–1) data were used for comparison with the X-ray images, whereas the ^{12}CO(J = 1–0) data was primarily used to estimate molecular mass from the integrated ^{12}CO intensity $W(^{12}\mathrm{CO})$ (K km s^{-1}) using the relationship $N(\mathrm{H_2}) = X_{\mathrm{CO}} \cdot [W(^{12}\mathrm{CO})\ (\mathrm{K\ km\ s^{-1}})]\ (\mathrm{cm^{-2}})$ with an X_{CO} factor of 2.0×10^{20} (cm^{-2} (K km s^{-1})$^{-1}$) (Bertsch et al. 1993).

We also used the data produced by Moriguchi et al. (2005). They observed the peaks A, C, and D with the ASTE sub-mm telescope in ^{12}CO(J = 3–2) in November 2004. These data were taken in position-switching mode with a 30″ grid spacing using a 23″ beam. An AOS spectrometer with a 450 km s^{-1} bandwidth and 0.43 km s^{-1} resolution was used. The system temperature was 300–400 K (DSB) and the typical rms achieved was 0.4–0.9 K with 30 s integration. The observed regions are shown in Fig. 2.1.

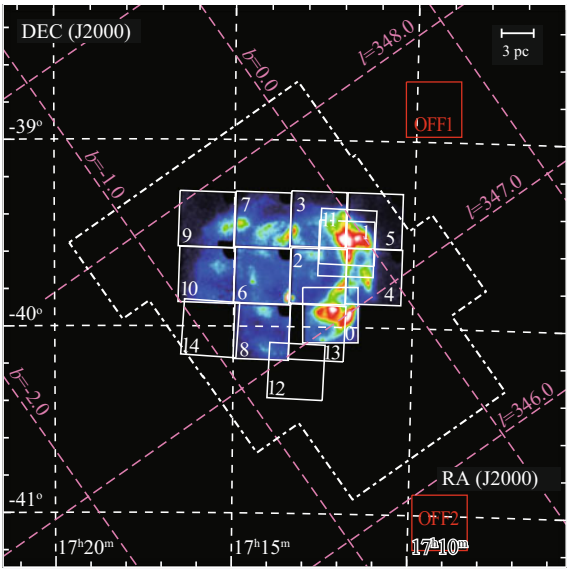

Fig. 2.1 *Suzaku* FoV of each observation of RX J1713.7−3946 overlaid on the *Suzaku* XIS 0+2+3 mosaic image (1–5 keV) taken from Tanaka et al. (2008). The small squares correspond to the FoV of the XIS. The numbers in the XIS FoV are pointing IDs used throughout this paper (see also Table 2.1). We also show the observed area in the ^{12}CO(J = 1–0, 2–1, 3–2, 4–3) and ^{13}CO(J = 2–1) enclosed by *white*, *red*, *green*, *yellow*, and *orange dash-dotted lines*, respectively

2.1.2 HI

The 21-cm HI spectral data were produced by the Southern Galactic Plane Survey (SGPS; McClure-Griffiths et al. 2005) using the Australia Telescope Compact Array (ATCA) combined with the 64-m Parkes Radio Telescope. The combined beam size and the grid spacing of the dataset are 2′.2 and 40″, respectively, and the velocity resolution and typical rms noise fluctuations are 0.82 km s^{-1} and 1.9 K, respectively. We applied a correction for HI self-absorption following the previous analysis of cold HI gas without CO emission (see Sect. 3.2.3.3).

2.1.3 X-Rays

We used *Suzaku* archive data of RX J1713.7−3946 taken from the Data Archives and Transmission System (DARTS at ISAS/JAXA). These observations comprising 15 pointings toward the main features and 2 OFF pointings of RX J1713.7−3946 and, excluding the four pointings observed in February 2010, were published by Takahashi et al. (2008) and Tanaka et al. (2008). Previous and current observations are summarized in Table 2.1, and the FoV of each observation is shown in Fig. 2.1. The *Suzaku* satellite has two active detector systems: the X-ray Imaging Spectrometer (XIS; Koyama et al. 2007) and the Hard X-ray Detector (HXD; Takahashi et al. 2007). The XIS comprises four CCD cameras, each of which is placed at the focus of an X-ray Telescope module (XRTs; Serlemitsos et al. 2007). For this work, we

Table 2.1 Summary of the *Suzaku* archive data of RX J1713.7−3946

Pointing ID	ObsID	α_{J2000} (^{h} ^{m} ^{s})	δ_{J2000} ($^{\circ}$ $'$ $''$)	XIS Exp. (ks)	Date	SCI
0.....	100026010	17 12 17.0	−39 56 11	69	September 26, 2005	OFF
1.....	501063010	17 11 51.5	−39 31 13	18	September 11, 2006	OFF
2.....	501064010	17 12 38.0	−39 40 14	21	September 11, 2006	OFF
3.....	501065010	17 12 38.2	−39 22 15	22	September 11, 2006	OFF
4.....	501066010	17 11 04.5	−39 40 10	21	September 12, 2006	OFF
5.....	501067010	17 11 05.1	−39 22 10	21	September 12, 2006	OFF
6.....	501068010	17 14 11.6	−39 40 14	21	September 13, 2006	OFF
7.....	501069010	17 14 11.4	−39 22 15	18	September 19, 2006	OFF
8.....	501070010	17 14 11.8	−39 58 14	21	September 19, 2006	OFF
9.....	501071010	17 12 17.6	−39 18 50	21	September 20, 2006	OFF
10.....	501072010	17 15 44.5	−39 40 10	20	October 5, 2006	OFF
11.....	504027010	17 11 50.8	−39 31 00	62	February 15, 2010	ON
12.....	504028010	17 13 14.0	−40 14 22	19	February 16, 2010	ON
13.....	504029010	17 12 39.8	−40 01 50	21	February 17, 2010	ON
14.....	504030010	17 15 39.0	−40 00 47	22	February 17, 2010	ON
OFF1.....	100026020	17 09 31.9	−38 49 24	35	September 25, 2005	OFF
OFF2.....	100026030	17 09 05.1	−41 02 07	38	September 28, 2005	OFF

Notes The details of pointing IDs from 0 to 10, OFF1, and OFF2 are also shown in Takahashi et al. (2008) and Tanaka et al. (2008)

analyzed only XIS data. The spaced-row charge injection (SCI; Nakajima et al. 2008; Uchiyama et al. 2009) was used in the latter four pointings (see also Table 2.1). Unfortunately, XIS 2 has been out of service since 9 November 2006, possibly owing to micrometeorite damage, and XIS 0 incurred anomaly in Segment A on June 23, 2009. Thus, to obtain data from the latter four pointings, we used XIS 0 (excluding data for Segment A), XIS 1, and XIS 3. To do so, we used "cleaned event files" that were processed and screened by versions 2.0 or 2.4 of the *Suzaku* pipeline depending on observation dates. We first created photon count images from the cleaned event files in the 1–5 and 5–10 keV energy bands, which were produced by subtracting the non-X-ray background (NXB) using **xisnxbgen**, which estimates the NXB count rate based on night time Earth observation data. We then corrected for XRT vignetting effects by simulating flat field images using **xissim** (Ishisaki et al. 2007). In addition, we masked calibration sources in the region of ^{55}Fe in the 5–10 keV energy band. Finally, we smoothed the images using a Gaussian kernel with a FWHM of 45″. We performed data reduction using version 6.11 of the HEAsoft tools.

2.2 Analysis

2.2.1 *Large-Scale CO, HI, and X-Ray Distributions*

Figure 2.2 shows mosaic images of RX J1713.7−3946 that were constructed by using data from XIS 0+1+2+3. Figure 2.2a and b show soft band (1–5 keV) and hard band (5–10 keV) images, respectively. The unit for the images is 10^{-4} counts s^{-1} $pixel^{-1}$ and the pixel size is $\sim 16\farcs7$. We find that the soft and hard band images are very similar, as was discussed in the previous study by Tanaka et al. (2008). Figure 2.2 clearly shows the western rim as well as several peaks of $\sim 10 \times 10^{-4}$ counts s^{-1} $pixel^{-1}$ in the northern rim and inside the SNR. In the soft band image,

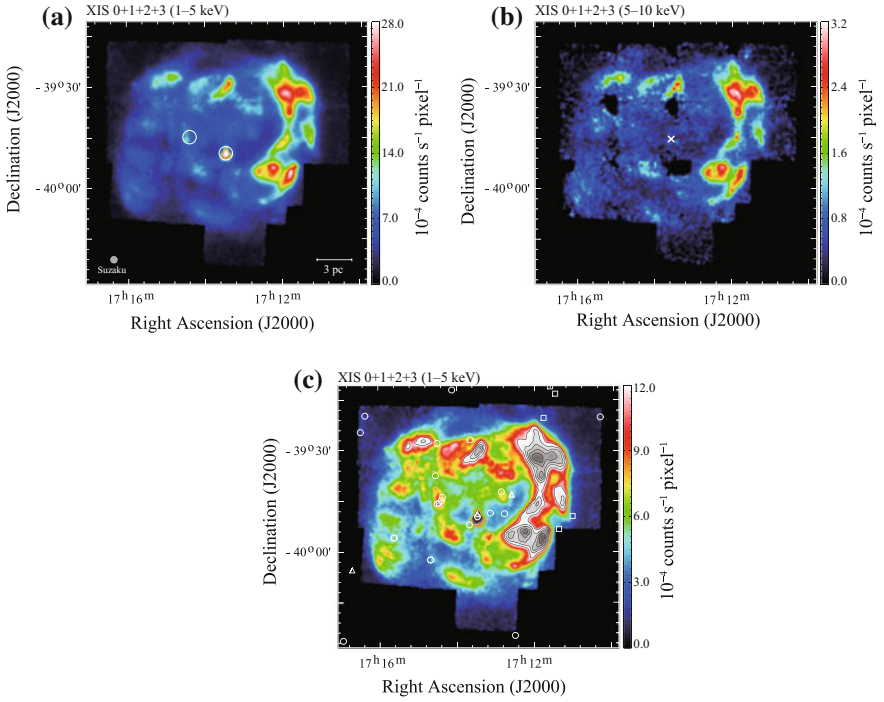

Fig. 2.2 *Suzaku* XIS (XIS 0+1+2+3) mosaic images of RX J1713.7−3946 in the **a** 1–5 keV and **b** 5–10 keV energy bands. The color scale indicates the count rate on a linear scale. The color bar numbers are in units of 10^{-4} counts s^{-1} $pixel^{-1}$ with a pixel size of $\sim 16\farcs7$. Both images are smoothed using a Gaussian kernel with an FWHM of 45″. The positions of the two point-like sources are shown with large circles in (**a**) (see Table 2.2). **c** Same XIS mosaic image (1–5 keV) as (**a**) but with the color scale changed to emphasize the region of low photon counts (below 12 × 10^{-4} counts s^{-1} $pixel^{-1}$). Regions above this level are shown in *gray* scale; the lowest contour level and the contour interval are 12 and 4 × 10^{-4} counts s^{-1} $pixel^{-1}$, respectively. The small *circles*, *triangles*, and *squares* show the position of seven X-rays point source, three pulsars, and two Wolf–Rayet stars, respectively

thick white circles indicate locations of the two bright point-like sources toward the inner part of the SNR. The left source is associated with a Wolf–Rayet star CD−39 11212B (Pfeffermann and Aschenbach 1996), which corresponds to two cataloged X-ray point sources (1WGA J1714.4−3945 and EXO 1710−396; see also Table 2.2). Owing to its X-ray spectral characteristics, the other source is thought to be a neutron star (Lazendic et al. 2003), which is cataloged as an X-ray point source (1WGA J1713.4−3949) and a pulsar (PSR J1713−3949). We also show a modified color scale image in the 1–5 keV energy band, which enhances the regions of the low photon count $\sim 7 \times 10^{-4}$ counts s^{-1} $pixel^{-1}$. In addition to the localized peaks in X-rays, we find diffuse X-ray emission extended within the SNR. To estimate the level of the background X-rays in the 1–5 keV X-ray image, we show two histograms of X-ray counts in Figure D1 (see Appendix D); one corresponds to the entire region observed by *Suzaku* (Fig. 2.1), whereas the other corresponds to nine $6'$ diameter circles without significant peaks inside the SNR (Figure D1). In the latter histogram, there is a peak at $\sim 3.86 \times 10^{-4}$ counts s^{-1} $pixel^{-1}$ that we identify as the background within the SNR. Similarly, we believe that a primary peak at $\sim 1.16 \times 10^{-4}$ counts s^{-1} $pixel^{-1}$ for the entire region indicates the background level outside the SNR. In Fig. 2.2c we plot the positions of the X-ray point sources, pulsars, and Wolf–Rayet stars (Table 2.2) in order to test whether the X-ray distribution is influenced by these point sources. As we see no excess in the regions around these point sources (except for the two bright point-like sources marked in the figure), we conclude that the X-ray features inside the SNR are not caused by the point sources but are intrinsic to the SNR.

Figure 2.3 shows four overlays of the ^{12}CO(J = 2–1) distribution and X-ray images in the 1–5 keV (Fig. 2.3a and b) and 5–10 keV (Fig. 2.3c and d) energy bands, respectively. A V_{LSR} range of CO from −20.2 to −9.1 km s^{-1} is shown in Fig. 2.3a and c and that from −9.1 to 1.8 km s^{-1} in Fig. 2.3b and d. These velocity ranges correspond to those of the interacting molecular gas (Fukui et al. 2012). Figure 2.3 indicates that CO and X-rays show good correlation at a pc scale, as already noted by Moriguchi et al. (2005). It is remarkable that most of the X-ray features are found toward CO clumps. The most outstanding X-ray flux is seen in the west of the shell, where the strongest CO emission is located (Fig. 2.3b and d); the second brightest X-ray regions are seen in the north of the shell, where CO emission is also distributed (Fig. 2.3a and c). The southern part of the CO emission appears to delineate the southern rim of the SNR (Fig. 2.3b and d), whereas the eastern shell with weak X-rays has only a few small CO features (Fig. 2.3b and d).

The CO distribution in the region of RX J1713.7−3946 is highly clumpy. To make a detailed comparison with the X-ray distribution, we cataloged CO clumps in the ^{12}CO(J = 1–0) data in Figure A1 in Appendix A. We identified 22 CO clumps in total, which were selected from the ^{12}CO(J = 1–0) data using the following three criteria: (1) the peak position is located within the SNR boundary, (2) the peak brightness temperature is higher than 1 K, and (3) the total clump surface area defined as the region surrounded by the contour at half of the maximum integrated intensity is larger than a three-beam area. We give the observed parameters of these clumps in ^{12}CO(J = 1–0) and ^{12}CO(J = 2–1) in Table 2.3. Thirteen of these are identified

Table 2.2 Summary of the X-ray point sources toward RX J1713.7−3946

Name	α_{J2000} ($^h\ ^m\ ^s$)	δ_{J2000} ($^\circ\ '\ ''$)	Source type	Ref.
2MASS J17110082−3949312	17 11 00.820	−39 49 31.22	Wolf–Rayet star	1
WR 84	17 11 21.70	−39 53 22.2	Wolf–Rayet star[a]	2
CD−39 11212B	17 14 27.129	−39 45 47.25	Wolf–Rayet star	1
2MASS J17112850−3913168	17 11 28.502	−39 13 16.88	Wolf–Rayet star	1
2MASS J17113611−3911079	17 11 36.118	−39 11 07.95	Wolf–Rayet star	1
2MASS J17114613−3920277	17 11 46.133	−39 20 27.78	Wolf–Rayet star	1
2MASS J17142712−3945472	17 14 27.129	−39 45 47.25	Wolf–Rayet star	1
PSR J1712−3943A	17 12 35.0	−39 43 14	pulsar	3
PSR J1712−3943B	17 12 35.0	−39 43 14	pulsar	3
PSR J1713−3949	17 13 28	−39 49.0	pulsar[a]	4
PSR J1716−4005	17 16 42.06	−40 05 27.0	pulsar	5
1RXS J171019.3−392006	17 10 19.298	−39 20 06.50	X-ray source	6
1RXS J171229.0−402459	17 12 28.997	−40 24 59.51	X-ray source	6
EXMS B1709−397A	17 12 46	−39 48.9	X-ray source	7
GPS 1709−396	17 12 51.0	−39 42 25	X-ray source	8
EXMS B1709−397B	17 13 08	−39 48.7	X-ray source	7
1WGA J1713.4−3949	17 13 28	−39 49.8	X-ray source[a]	4, 9
2XMM J171338.9−392658	17 13 38.91	−39 26 58.4	X-ray source	10
CXOPS J171340.5−395213	17 13 40.5	−39 52 13	X-ray source	11
AX J1714.1−3912	17 14 07.0	−39 12 12	X-ray source	12
EXO 1710−396	17 14 22	−39 44.0	X-ray source[b]	13
1WGA J1714.4−3945	17 14 24	−39 45	X-ray source[b]	14, 15
2XMM J171429.6−394559	17 14 29.72	−39 45 59.8	X-ray source	10
2XMM J171429.7−392801	17 14 29.74	−39 28 01.5	X-ray source	10
CXOU J171432.4−393735	17 14 32.48	−39 37 35.3	X-ray source	16
CXOPS J171440.6−400234	17 14 40.6	−40 02 34	X-ray source	11
2XMM J171440.7−400232	17 14 40.7	−40 02 32	X-ray source	10
CXOPS J171537.1−395559	17 15 37.1	−39 55 59	X-ray source	11
2XMM J171537.0−395559	17 15 37.0	−39 55 59	X-ray source	10
1RXS J171620.2−391946	17 16 20.201	−39 19 46.49	X-ray source	6
1RXS J171627.5−392439	17 16 27.502	−39 24 39.49	X-ray source	6
1RXS J171657.1−402627	17 16 57.101	−40 26 26.99	X-ray source	6

Notes [a] and [b] sources are connected with two X-ray point-like sources shown in Fig. 2.2, respectively. (1) Cutri et al., 2003; (2) van der Hucht, 2001; (3) Burgay et al., 2006; (4) Lazendic et al., 2003; (5) Eatough et al., 2013; (6) Voges et al., 1999; (7) Reynolds et al., 1999; (8) Gottwald et al., 1995; (9) Landt and Bignall, 2008; (10) Lin et al., 2012; (11) van den Berg et al., 2012; (12) Uchiyama et al., 2002; (13) Lu et al., 1996; (14) Slane et al., 1999; (15) Pfeffermann and Aschenbach, 1996; (16) Guillot et al., 2009

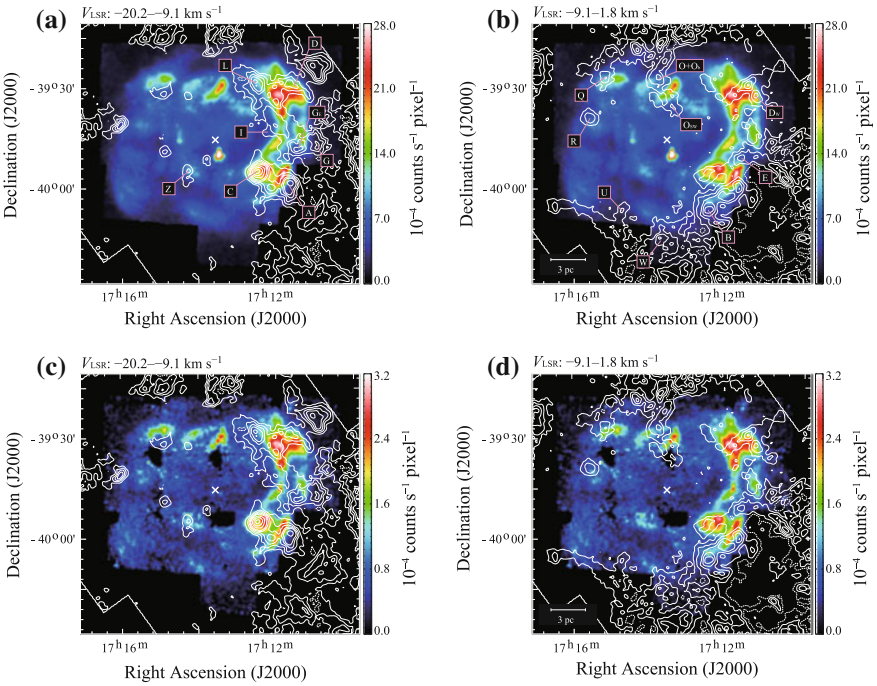

Fig. 2.3 Pair of ^{12}CO($J = 2$–1) velocity channel maps (*white contours*) superimposed on the *Suzaku* XIS mosaic image in two energy bands (**a**, **b**: 1–5 keV and, **c**, **d**: 5–10 keV) in color scale. The velocity ranges are **a**, **c** −20.2–−9.1 km s^{-1} and **b**, **d** −9.1–1.8 km s^{-1}, respectively. The lowest contour level and the contour interval of CO are 3.1 K km s^{-1} ($\sim 3\sigma$) in **b** and **d**, respectively. In **a** and **c**, the contour levels are 3.1, 6.2, 9.3, 12.4, 15.5, 21.7, 27.9, and 31.0 K km s^{-1}. The CO clumps discussed in Sect. 2.2.2 are indicated in the figure

either by Fukui et al. (2003) or Moriguchi et al. (2005); the rest are newly identified in the present work. Most of the CO clumps have a single velocity component of line width ∼3–5 km s^{-1}. Only clump O (Moriguchi et al. 2005) has two velocity components with ∼7.5 km s^{-1} separation, and it is divided into two clumps, O and O$_b$. Five of the clumps D$_W$, G$_E$, O$_b$, O$_{SW}$, and Z have molecular mass higher than 50 $M_\odot$ (see also Table 2.3), whereas four of them C$_E$, Q$_W$, Z$_{NW}$, and Z$_{NE}$ have molecular mass less than 50 $M_\odot$. We focus hereafter on the 18 CO clumps having molecular mass greater than 50 $M_\odot$, as shown in Fig. 2.3, to ensure consistent derivation of physical parameters for a quantitative comparison with the X-ray characteristics (Sect. 2.1.3). Except for the five clumps C, I, L, O$_{SW}$, and Z, which are located inside the SNR boundary, most of the clumps (A, B, D, D$_W$, E, G, G$_E$, O, O$_b$, Q, R, U, and W) are distributed on the outer boundary of the SNR shell.

Finally, we compare the cold HI gas without CO with the X-rays in the southeastern rim of the SNR (hereafter SE rim; see Sect. 3.2.3.3). The cold HI gas has a density of around 100 cm^{-3} and is likely interacting with the shock in a similar way to the CO.

Table 2.3 Properties of CO clumps

Name (1)	^{12}CO($J = 1$–0)						^{12}CO($J = 2$–1)				
	α_{J2000} (^{hms}) (2)	δ_{J2000} ($^{\circ\prime\prime\prime}$) (3)	T_{R^*} (K) (4)	V_{peak} (km s^{-1}) (5)	ΔV_{LSR} (km s^{-1}) (6)	Mass ($M_\odot$) (7)	α_{J2000} (^{hms}) (8)	δ_{J2000} ($^{\circ\prime\prime\prime}$) (9)	T_{R^*} (K) (10)	V_{peak} (km s^{-1}) (11)	ΔV_{LSR} (km s^{-1}) (12)
A.....	17 11 35.9	−39 59 01.8	8.5	−10.3	4.8	686	17 11 38.4	−39 58 46.9	6.6	−10.0	4.5
B.....	17 12 26.5	−40 06 06.3	4.2	−8.0	4.6	190	17 12 26.8	−40 05 55.5	3.3	−8.1	4.5
C.....	17 12 25.9	−39 56 04.4	9.4	−12.0	3.8	397	17 12 27.0	−39 54 58.0	7.5	−11.9	4.6
$C_{E.....}$	17 13 01.3	−39 53 35.2	1.1	−9.1	1.6	10	17 12 57.4	−39 53 42.3	3.7	−8.8	1.4
D.....	17 11 28.0	−39 30 37.6	4.0	−11.1	4.8	292	17 11 32.5	−39 30 03.9	3.3	−9.3	4.8
$D_{W.....}$	17 11 01.3	−39 34 17.6	2.3	2.4	3.3	137	17 11 34.3	−39 32 31.2	3.1	−1.1	6.0
E.....	17 11 29.1	−39 50 38.5	2.0	−6.1	7.2	159	17 11 55.4	−39 51 07.2	2.0	−6.0	5.0
G.....	17 10 55.6	−39 45 55.2	3.3	−10.8	8.0	307	17 10 56.3	−39 45 20.6	2.8	−11.5	4.8
$G_{E.....}$	17 11 27.1	−39 47 49.6	5.4	−12.8	2.6	168	17 11 21.0	−39 47 24.4	4.3	−12.3	2.7
I.....	17 12 08.2	−39 43 43.3	1.8	−9.9	5.4	103	17 12 16.6	−39 43 22.8	1.3	−10.4	5.9
L.....	17 12 25.8	−39 28 53.4	4.0	−12.0	5.7	370	17 12 30.2	−39 28 14.6	3.2	−11.7	6.0
O.....	17 13 46.7	−39 27 49.8	1.1	−6.4	4.9	61	17 13 46.0	−39 26 28.6	1.2	−4.6	4.7
$O_{b.....}$	17 13 46.7	−39 27 49.8	1.9	1.1	3.4	80	17 13 46.0	−39 26 28.6	1.9	1.0	3.8
$O_{SW.....}$	17 13 24.8	−39 37 08.6	2.8	−1.6	2.0	60	17 13 08.9	−39 36 43.2	3.5	−1.3	1.3

(continued)

Table 2.3 (continued)

Name (1)	^{12}CO(J = 1–0)						^{12}CO(J = 2–1)				
	α_{J2000} (^{hms}) (2)	δ_{J2000} ($^{\circ\prime\prime\prime}$) (3)	T_{R^*} (K) (4)	V_{peak} (km s^{-1}) (5)	ΔV_{LSR} (km s^{-1}) (6)	Mass ($M_\odot$) (7)	α_{J2000} (^{hms}) (8)	δ_{J2000} ($^{\circ\prime\prime\prime}$) (9)	T_{R^*} (K) (10)	V_{peak} (km s^{-1}) (11)	ΔV_{LSR} (km s^{-1}) (12)
Q.....	17 15 13.4	−39 25 06.2	2.9	−2.8	3.2	108	17 15 11.7	−39 26 47.4	2.8	−2.2	2.8
Q$_{W.....}$	17 14 49.3	−39 31 35.1	3.0	−14.3	2.4	46	17 14 53.0	−39 31 30.7	3.7	−14.1	1.8
R.....	17 15 39.9	−39 38 34.6	4.1	−3.3	2.4	67	17 15 32.0	−39 39 28.5	3.2	−3.1	2.2
U.....	17 14 34.2	−40 06 27.0	3.7	−4.8	1.3	58	17 14 13.4	−40 06 25.2	3.0	−4.6	1.3
W.....	17 13 42.8	−40 16 40.7	5.0	−5.1	3.0	402	17 13 30.0	−40 15 03.6	3.3	−4.9	3.4
Z.....	17 14 18.7	−39 56 55.1	2.6	−20.1	2.7	72	17 13 53.3	−39 54 46.8	2.9	−19.8	2.9
Z$_{NW....}$	17 13 45.0	−39 52 14.9	3.0	−19.8	2.6	36	17 13 45.6	−39 51 09.2	5.1	−19.8	1.8
Z$_{NE.....}$	17 14 57.4	−39 49 59.3	2.2	−20.0	3.3	31	17 14 53.3	−39 49 25.7	3.6	−19.6	2.5

Notes Col. (1): Clump name. Cols. (2–7) and (8–12): Observed properties of the ^{12}CO(J = 1–0, 2–1) spectra obtained at the peak positions of the CO clumps. Cols. (2)–(3): Position of the peak CO intensity. Col. (4): Peak radiation temperature T_{R^*}. Col. (5): V_{peak} derived from a single Gaussian fitting. Col. (6): FWHM line width ΔV_{LSR}. Col. (7): Total mass of the clumps derived using the relation between the molecular hydrogen column density $N(H_2)$ and the ^{12}CO(J = 1–0) intensity $W(^{12}CO)$, $N(H_2) = 2.0 \times 10^{20}[W(^{12}CO)$ (K km s^{-1})] (cm^{-2}) (Bertsch et al. 1993). See the text for more details. Cols. (8–12): The observed properties, same as Cols. (2–6) for the ^{12}CO(J = 2–1) spectra. The properties of A–E, G, I–O, and Q–W derived from ^{12}CO(J = 1–0) are shown by Moriguchi et al. (2005)

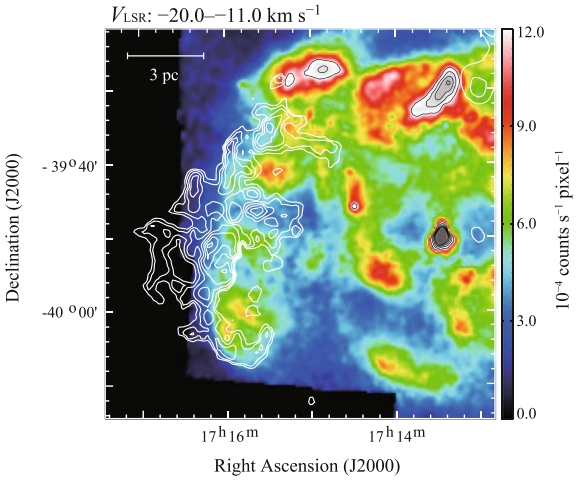

Fig. 2.4 Same XIS mosaic image (1–5 keV) as Fig. 2.2c toward the SE rim. The *white* contours indicate the distribution of HI proton column density (self-absorption corrected; see Sect. 3.2.3.3). The lowest contour level and the contour interval in HI proton column density are 2.0 and 0.1 × 10^{21} cm^{-2}, respectively. The velocity range is −20.0 to −11.0 km s^{-1}

Figure 2.4 shows an enlarged view in the SE rim overlaid with the HI proton column density contours with an integration range of −20.0 to −11.0 km s^{-1}. We applied HI self-absorption by following the analysis in Sect. 3.2.3.3. The lowest contour level and the contour interval in the HI proton column density are 2.0 × 10^{21} cm^{-2} and 0.1 × 10^{21} cm^{-2}, respectively. It is remarkable that the HI distribution corrected for the self-absorption is complementary to the X-ray peaks in the low-photon-count region in the SE rim.

2.2.2 *Detailed Comparison with X-Ray Data*

We here make a detailed comparison of the spatial distributions of the CO/HI clumps with those in the X-ray images in terms of radial and azimuthal distributions.

In Fig. 2.5, the left and middle panels of each row show images of the CO integrated intensity overlaid onto the distributions of soft band (1–5 keV, left) and hard band (5–10 keV, middle) X-rays. The crosses in each image indicate the centers of gravity of the CO clumps listed in Table 2.4, which are somewhat different from the peak positions listed in Table 2.2, and each arrow indicates the direction of the center of the SNR. The dashed white circles represent radii 0.°06 and 0.°12 of the center of gravity. We see a trend wherein X-ray intensity is enhanced toward the CO clumps, although the CO peaks generally show offsets from the X-ray peaks. In the right panels of Fig. 2.5, we plot radial profiles of the CO integrated intensity and X-ray counts averaged at each radius for the 1–5 and 5–10 keV bands. To quantitatively characterize the radial distribution, we first identify the peak in the 1–5 keV radial distribution. In addition, we defined the separation between the center of gravity of the CO clumps and that of the X-ray peaks in the radial distribution. Ten of the 17

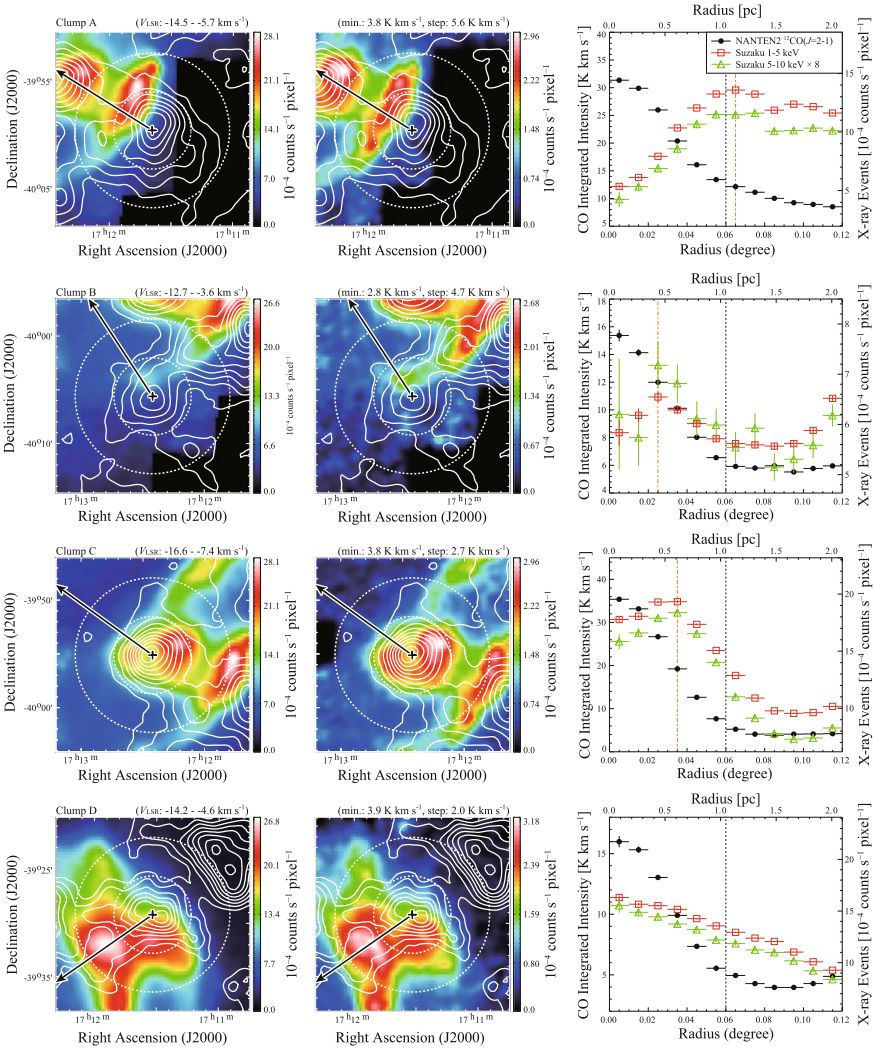

Fig. 2.5 Distribution of ^{12}CO($J=$ 2–1) emission (*white contours*) superimposed on the *Suzaku* 1–5 keV (*left*) and 5–10 keV (*middle*) images. Velocity range in integration and contour levels are shown in the *top of left* and *middle panels*, respectively. Each *arrow* indicates the direction of the center of the SNR. The crosses show the position of the center of gravity for each CO clump (see also Table 2.4). The *dashed white circles* represent radii 0.°06 and 0.°12 of the center of gravity for each CO clump. *Right panels* show the radial profiles around each molecular clump in the ^{12}CO(J=2–1) integrated intensity and the two *Suzaku* energy bands (1–5 keV and 5–10 keV, in units of 10^{-4} counts s^{-1} pixel^{-1}) in Fig. 2.2. The radial profiles from the 5–10 keV band have been scaled such that they has the same area as the 1–5 keV profiles (scaled by a factor 8), for the sake of direct comparison. The *orange dash-dotted lines* indicate X-ray peak radius in the 1–5 keV energy band

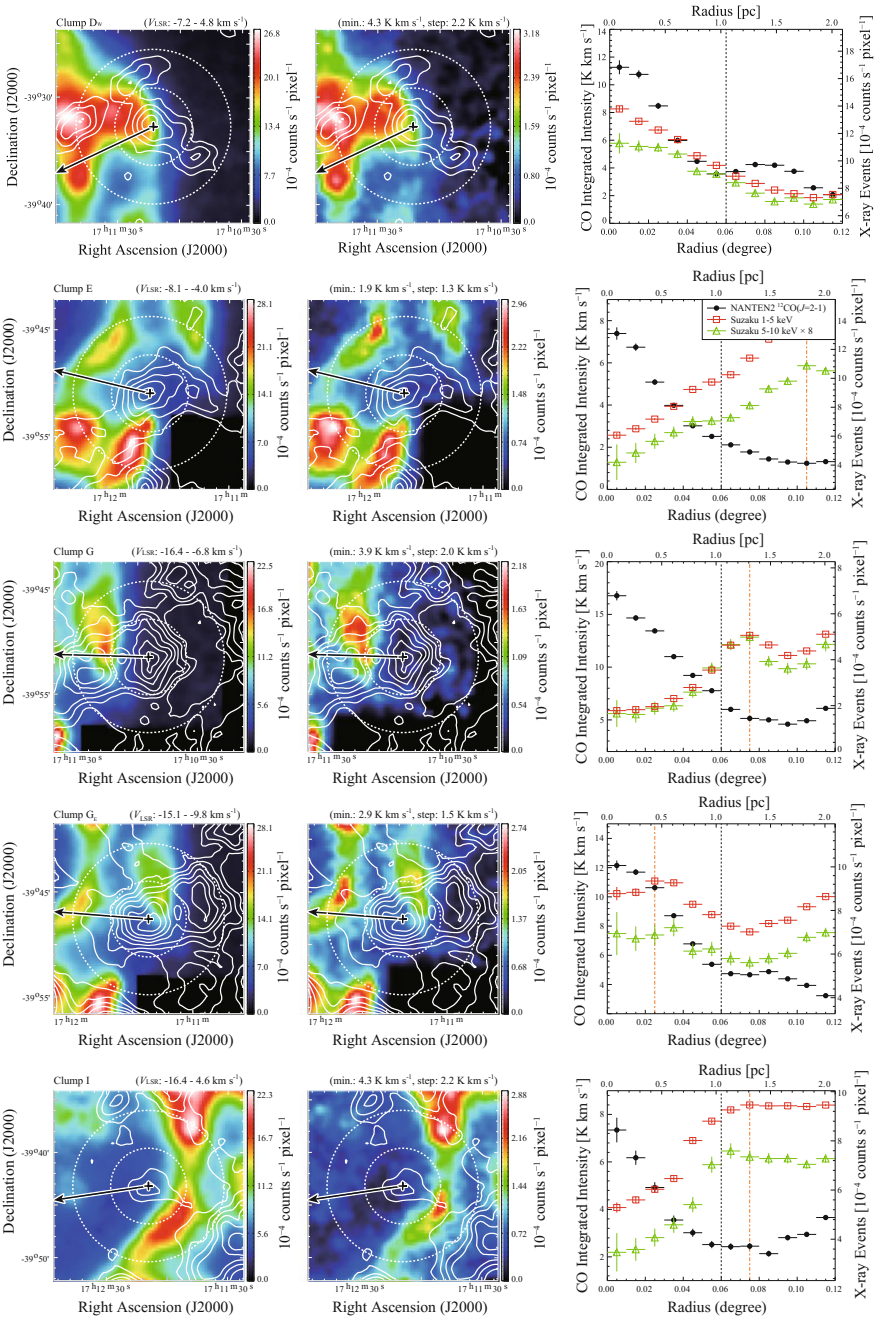

Fig. 2.5 (continued)

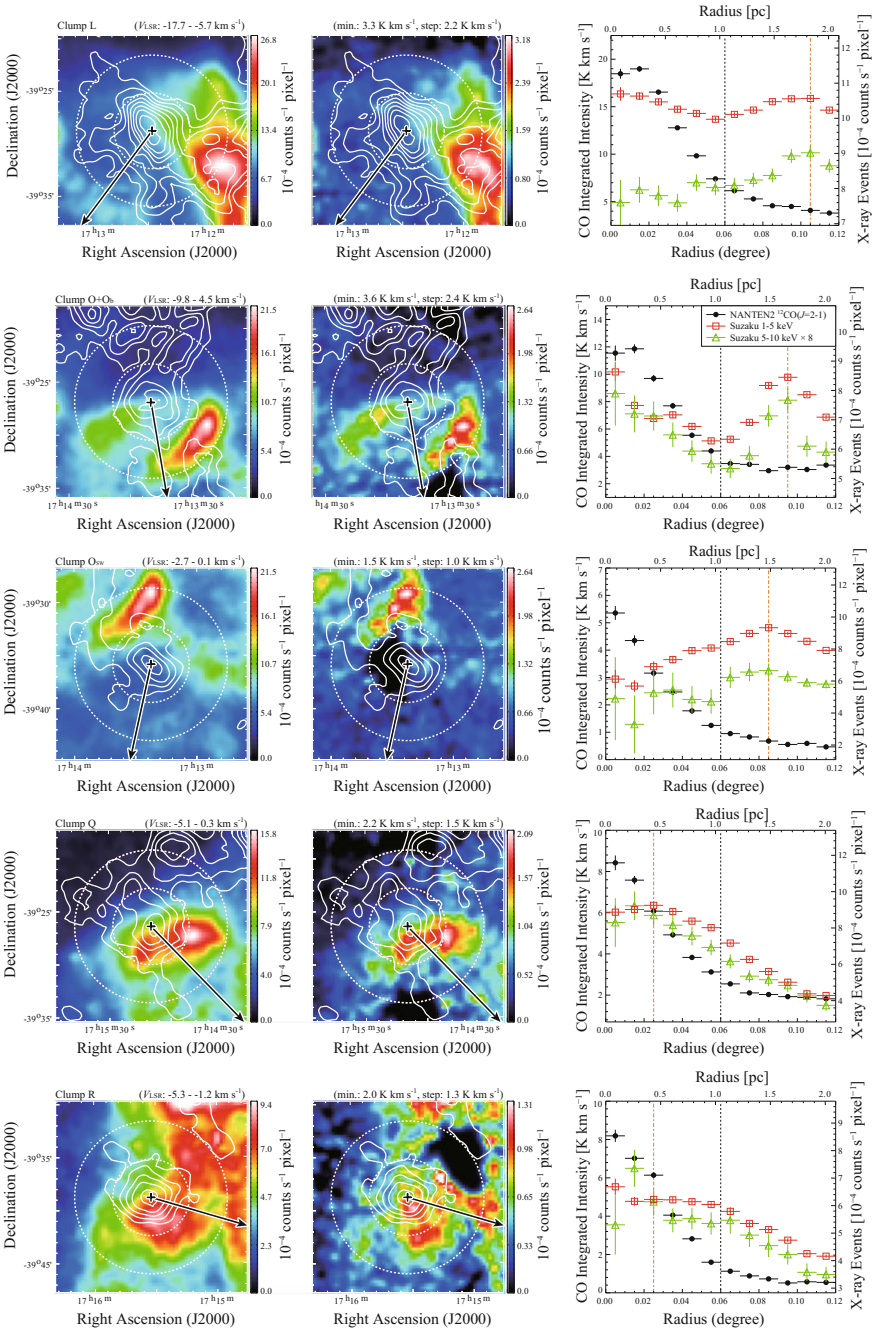

Fig. 2.5 (continued)

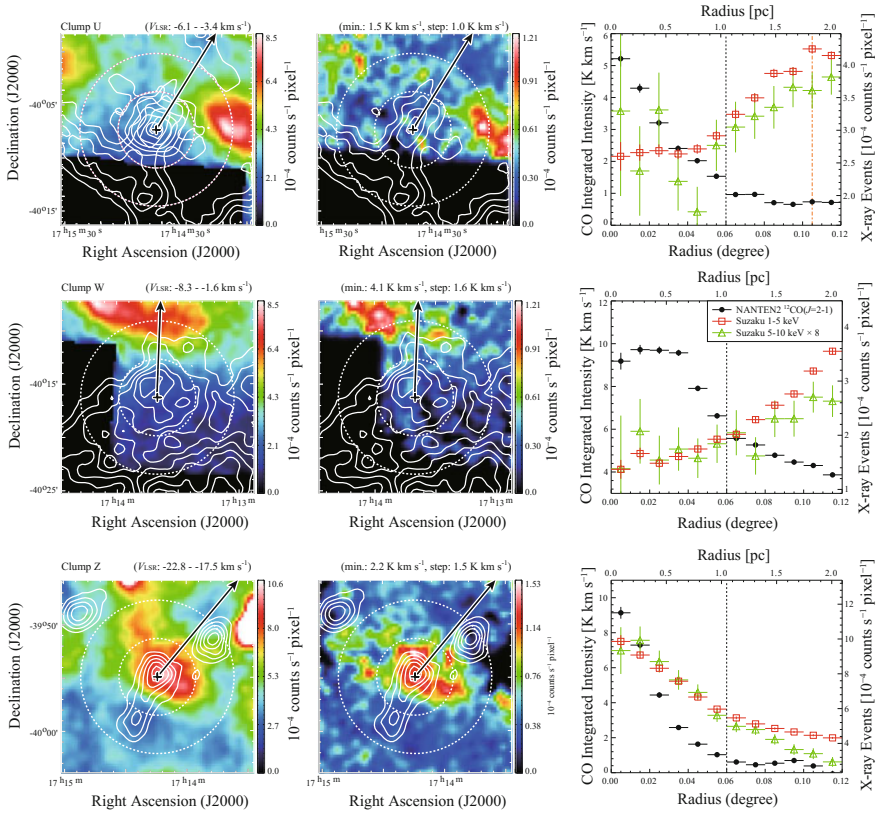

Fig. 2.5 (continued)

Table 2.4 Results of radial and azimuthal distribution

Name (1)	α_{J2000} (^{h} ^{m} ^{s}) (2)	δ_{J2000} ($^\circ$ $'$ $''$) (3)	V_{LSR} (km s^{-1}) (4)	Radius (degree) (5)	Separation (degree) (6)	Peak Intensity ($\times 10^{-4}$ counts s^{-1} pixel) (7)	Angle (Fraction) (degree), (%) (8)	Interacting Mass ($M_\odot$) (9)
A.....	17 11 39.1	−39 59 22.2	−14.5–−5.7	0.050	0.065	18.50 ± 0.07	−120–+120, (67)	460 ± 60
B.....	17 12 25.3	−40 05 37.5	−12.7–−3.6	0.050	0.025	10.88 ± 0.05	−150–+90, (67)	130 ± 20
C.....	17 12 25.3	−39 55 07.4	−16.6–−7.4	0.040	0.035	19.64 ± 0.07	−180–+180, (100)	400 ± 30
D.....	17 11 31.9	−39 29 13.6	−14.2–−4.6	0.040	···	22.25 ± 0.07	−150–+150, (83)	240 ± 20
Dw.....	17 11 12.8	−39 32 43.5	−7.2–4.8	0.040	···	21.18 ± 0.07	−120–+90, (58)	80 ± 11
E.....	17 11 38.7	−39 50 56.8	−8.1–−4.0	0.040	0.105	19.81 ± 0.07	−180–+180, (100)	159 ± 13
G.....	17 10 54.5	−39 46 25.7	−16.4–−6.8	0.050	0.075	11.81 ± 0.09	−60–+60, (33)	100 ± 30
GE.....	17 11 22.2	−39 47 34.0	−15.1–−9.8	0.050	0.025	13.16 ± 0.13	−150–+150, (83)	140 ± 14
I.....	17 12 09.3	−39 43 11.9	−16.4–−4.6	0.030	0.075	14.22 ± 0.07	−180–+180, (100)	103 ±9
L.....	17 12 28.2	−39 28 45.9	−17.7–−5.7	0.045	0.105	19.91 ± 0.07	−180–+180, (100)	370 ± 30
O.....	17 13 48.9	−39 26 24.9	−11.3–−1.6	0.055	0.095	14.02 ± 0.14	−120–+120, (67)	41 ±5
Ob.....	17 13 46.9	−39 26 45.9	−4.6–2.2	0.035	0.085	13.92 ± 0.14	−120–+120, (67)	53 ±7

(continued)

Table 2.4 (continued)

Name (1)	α_{J2000} (^{h} ^{m} ^{s}) (2)	δ_{J2000} ($^\circ$ $'$ $''$) (3)	V_{LSR} (km s^{-1}) (4)	Radius (degree) (5)	Separation (degree) (6)	Peak Intensity ($\times 10^{-4}$ counts s^{-1} pixel) (7)	Angle (Fraction) (degree), (%) (8)	Interacting Mass ($M_\odot$) (9)
Osw.....	17 13 22.4	−39 35 50.6	−2.7–0.1	0.030	0.085	14.5± 0.2	−180–+180, (100)	60 ±5
Q.....	17 15 09.6	−39 38 48.7	−5.1–0.3	0.040	0.025	10.83 ± 0.12	−150–+120, (75)	81 ±9
R.....	17 15 32.4	−39 39 28.5	−5.3–−1.2	0.035	0.025	6.7± 0.2	−150–+150, (83)	56 ±6
U.....	17 14 44.5	−40 07 24.4	−6.1–−3.4	0.030	0.105	5.54 ± 0.07	−90–0, (25)	15 ±5
W.....	17 13 40.2	−40 16 16.9	−8.3–−1.6	0.080	···	4.58 ± 0.07	−30–+30, (17)	70 ± 30
Z.....	17 14 14.3	−39 54 55.7	−22.8–−17.5	0.025	···	3.60 ± 0.06	−150–+180, (92)	66 ±6
HI SE rim.....	17 16 09.3	−40 03 10.6	−20.0–−11.0	···	···	6.97 ± 0.09	−90–+60, (42)	56 ± 11
O+Ob.....	17 13 49.7	−39 26 54.9	−9.8–4.5	0.040	0.095	14.03 ± 0.14	−120–+120, (67)	94 ±8
D+Dw.....	···	···	···	···	···	21.72 ± 0.05	···	320 ± 30
O+Ob+Osw.	···	···	···	···	···	14.19 ± 0.09	···	154 ± 10
G+GE.....	···	···	···	···	···	12.49 ± 0.08	···	240 ± 30
E+I.....	···	···	···	···	···	17.02 ± 0.05	···	260 ± 20

Notes Col. (1): Clump name. Cols. (2)–(3): Position of the center of gravity with the ^{12}CO(J = 2–1) integrated intensity (except for the SE rim). Cols. (4): Integration range of velocity for the estimation of the ^{12}CO(J = 2–1) or HI. (5): Radius of a CO clump defined as the radial distance from the center of gravity of the clump to the point where the intensity is at half maximum. (6) Separation of the X-ray peak from the center of gravity of each CO/HI clump. (7) X-ray peak intensity with the statistical error around each clump shown in Fig. 2.8. (8) Azimuth angle range of the X-rays (1–5 keV) above the background level estimated in Appendix A (see also Sect. 2.2.1). (9) Interacting clump mass defined as the total CO/HI mass within the azimuth angle range of the X-rays (1–5 keV) for each clump.

clumps have X-ray peaks and positive X-ray slopes inside the peak in Fig. 2.5. Clump W has no peak and shows a clear positive X-ray slope. On the other hand, four of the CO clumps show negative slopes and the other shows a nearly flat slope. As the radial distributions of the X-ray peaks are generally smooth and monotonic, linear approximation is reasonable for estimating intensity gradients. Only the CO clumps O+O$_b$ show a complicated, non-monotonic radial distribution of X-ray peaks, which may be caused by a blending of the two velocity components. We made least-squares fits to the X-ray peak distributions using a straight line for simplicity for the 10 clumps within the peak, and for clump W and the other six clumps within a radius of 0.°06. The respective slope values are listed in Table 2.5 and are shown as a histogram in Fig. 2.6. Twelve of the 16 clumps (75%) show positive slopes, indicating that the X-rays show a decrease toward the CO clump and are brighter in the neighborhood of the clump. With the exception of clump Z, the four clumps with negative or flat slopes also show a clear relative enhancement of X-rays in their vicinities (in Fig. 2.5 left and middle panels). Clump Z has no clear X-ray depression toward the center, whereas enhanced X-rays are seen in its surroundings (Fig. 2.5 left and middle panels

Table 2.5 Fitting results of the X-rays radial distribution

Name (1)	Fitting range (degree) (2)	Slope ($\times 10^{-4}$ counts s^{-1} pixel degree^{-1}) (3)	Comments (4)
A.....	0.00–0.07	+152 ±2	Positive slope with peak
B.....	0.00–0.03	+40 ±10	Positive slope with peak
C.....	0.00–0.04	+56 ±6	Positive slope with peak
D.....	0.00–0.06	−59 ±2	Negative slope
Dw.....	0.00–0.06	−84 ±3	Negative slope
E.....	0.00–0.11	+82 ±1	Positive slope with peak
G.....	0.00–0.08	+57 ±1	Positive slope with peak
GE.....	0.00–0.03	+40 ± 20	Positive slope with peak
I.....	0.00–0.08	+70 ±2	Positive slope with peak
L.....	0.00–0.10	+2 ±1	Flat
O+Ob.....	...	...	...
Osw.....	0.00–0.09	+43 ±3	Positive slope with peak
Q.....	0.00–0.03	+20 ± 20	Positive slope with peak
R.....	0.00–0.03	−10 ± 10	negative slope
U.....	0.00–0.10	+19 ±1	Positive slope with peak
W.....	0.00–0.06	+10 ±2	Positive slope with no peak
Z.....	0.00–0.06	−79 ±4	Negative slope

Notes Col. (1): Clump name. Col. (2): Fitting range of X-rays in radial plot (see also the text for details). Col. (3): Slope of least-squared fitted straight line of X-rays with 1 sigma error. (4) Comments.

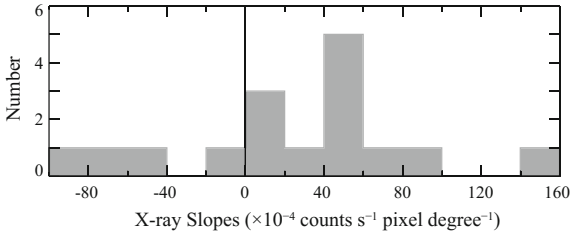

Fig. 2.6 Histogram of the X-ray slope estimated by linear fitting to the radial profile for each CO clump. The fitting ranges and results are shown in Table 2.5

in the last low). We conclude that the enhancement of X-rays around a clump are a general trend among the CO clumps. We note that, on average, each CO clump has a radius of $0.^{\circ}04 \pm 0.^{\circ}01$ and that X-ray peaks are distributed with a separation $0.^{\circ}07 \pm 0.^{\circ}03$ from the center of each clump (see also Table 2.4).

We performed a similar analysis of the cold HI in the SE rim. The HI distribution estimated from self-absorption clearly delineates the outer boundary of the X-rays (Fig. 2.7) and the relative distributions are similar to those for clump A. The HI column density distribution is fairly flat and has no clear peak. Thus, instead of using the HI peak, we draw a line passing through the center of the SNR and the soft X-ray peak, and then, we define the HI column density peak on the line. The radial distributions are plotted centered on this HI peak. We find a trend similar to that of the CO clumps wherein the X-rays are clearly enhanced around the cold HI.

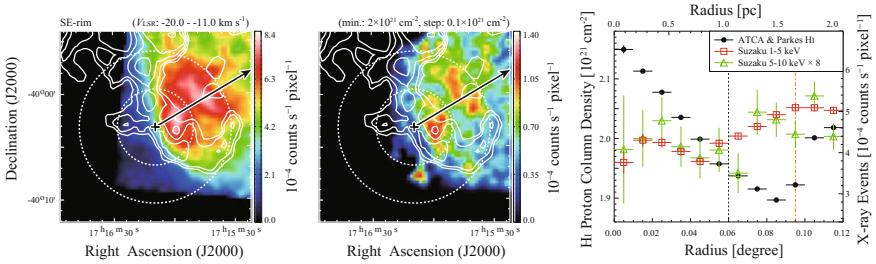

Fig. 2.7 Distribution of the cold HI column density (*white contours*) superimposed on the *Suzaku* images in the 1–5 (*left*) and 5–10 keV (*middle*) bands. Velocity range of integration and contour levels are shown in the *top of the left* and *middle panels*, respectively. Each *arrow* indicates the direction of the center of the SNR passing through the X-ray peak in the 1–5 keV image. The *crosses* show the position representing the cold HI clump and is determined as the crossing point of the HI cloud with the arrow, $(\alpha_{J2000}, \delta_{J2000}) = (17^{h}\ 16^{m}\ 9.3^{s}, -40^{\circ}\ 3'\ 10.6'')$ (also see the text). The *dashed white circles* represent radii of $0.^{\circ}06$ and $0.^{\circ}12$ centered on the crosses. *Right panel* shows the radial profile around the crosses in the HI column density and the X-ray counts in the two energy bands (1–5 and 5–10 keV) in Fig. 2.2. The radial profile in the 5–10 keV band is scaled by a factor of 8 relative to the 1–5 keV band for the sake of direct comparison. The *orange dash-dotted line* indicates the X-ray peak radius in the 1–5 keV band

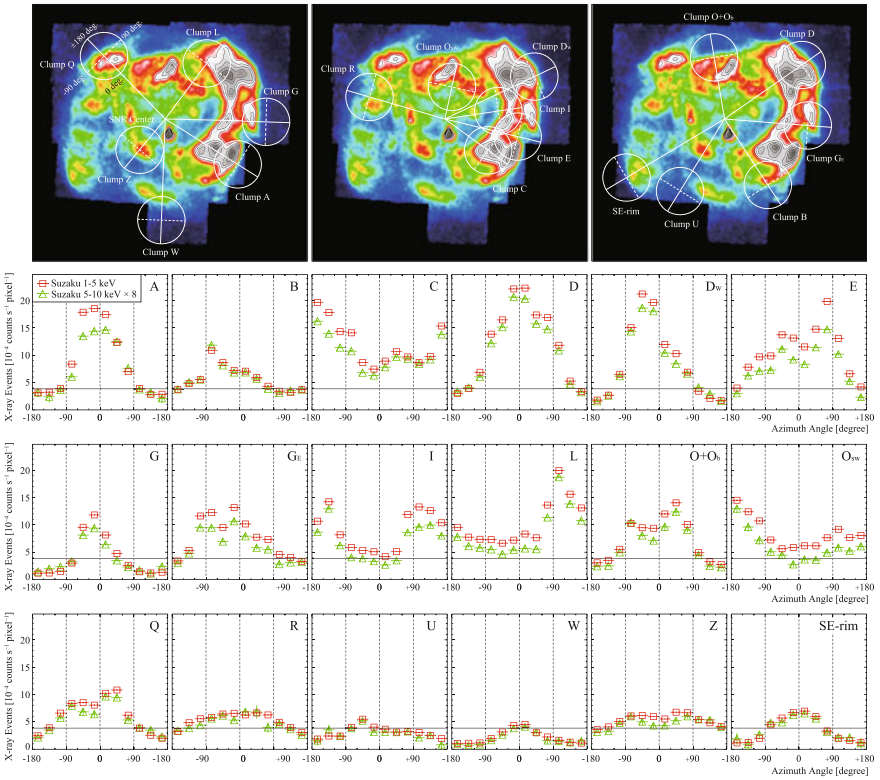

Fig. 2.8 *Top panels* Same XIS mosaic image (1–5 keV) as in Fig. 2.2c. Overlaid *white circles* are centered on the center of gravity of each CO/HI clump. The azimuthal distribution of X-rays is averaged within each circle (radius = 0.°12). Each *white* solid straight line connects the centers of the circle and the SNR and each *dashed white line* in the circle is vertical to the solid line. The azimuthal angle is measured using the solid line as the origin counterclockwise from −180° to 180° (e.g., clump Q in *top panel*). *Other panels* Azimuthal distributions of *Suzaku* XIS 1–5 keV (*red square*) and 5–10 keV (*green triangles* are scaled by a factor of eight) averaged in the circles for each clump. The *horizontal solid lines* indicate the background level of the X-rays estimated inside the SNR for the 1–5 keV energy band (see the text)

In Fig. 2.8, the top three panels show the same XIS mosaic images (1–5 keV) as those in Fig. 2.2c. The lines connecting the CO/HI clump positions (shown in Figs. 2.5 and 2.7 and in Table 2.4) and the center of the SNR $(l, b) = (347.^{\circ}3, -0.^{\circ}5)$ or $(\alpha_{J2000}, \delta_{J2000}) = (17^{h}\ 13^{m}\ 34^{s}, -39^{\circ}\ 48'\ 17'')$ are taken as the origins of the azimuth angle, which is measured counterclockwise. The azimuthal angular distribution of the X-rays around each CO/HI clump is estimated with respect to the direction of the center of the SNR. We measured the azimuthal angular extent of the X-rays in each clump in the 1–5 keV band image by adopting the background level inside the SNR as the threshold (Sect. 2.2.1). The results are shown in Fig. 2.8 and Table 2.4. The upper panel of Fig. 2.9 shows the range of angles and the lower panel shows a

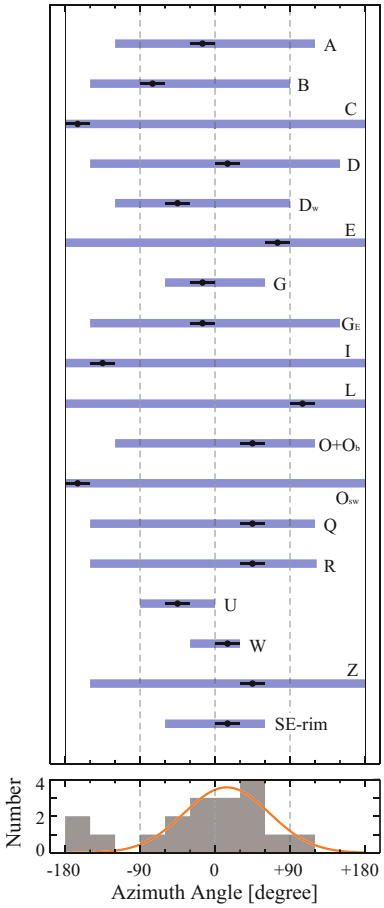

Fig. 2.9 The azimuthal angular extent of the X-rays above the background level in each CO/HI clump for the 1–5 keV band image (*top panel*; see also Table 3). Each *black dot* indicates the angle of X-ray peak intensities in Fig. 2.8. The histogram of the X-ray peak positions is shown in the *lowest panel*. The *red curve* indicates the fitting result by a Gaussian function for the clumps from $-90°$ to $+120°$

histogram of the peak angles. The five clumps inside the SNR, clumps C, E, I, L, and O_{SW}, are fully surrounded by the X-rays, which show a peak toward the azimuthal angle of $-180°$ to $-120°$ (clumps C, I, and O_{SW}) or $+60°$ to $+120°$ (clumps E and L). These distributions indicate that the clumps inside the SNR are surrounded by enhanced X-rays, whereas those on the border of the SNR have enhanced X-rays only toward the center of the SNR. In Fig. 2.9, lower panel, we see a trend that the X-ray intensity is enhanced at an azimuthal angle of around $0°$ and scattering is high, $\pm 60°$ (clumps A, D, D_W, G, G_E, O+O_b, Q, R, U, W, Z, and SE rim). The histogram was fitted by a Gaussian function from $-120°$ to $120°$, and we find that the best-fit parameters of center and sigma are $14° \pm 5°$ and $51° \pm 5°$, respectively.

2.2.3 Sub-Millimeter Results; $^{12}CO(J = 4–3)$ Distribution

We observed the $^{12}CO(J = 4–3)$ transition in a region of $3'.0 \times 3'.0$ in equatorial coordinates around clump C and toward the peak position of Clump A. Figure 2.10 shows four images of clump C in the $^{12}CO(J = 2–1, 3–2,$ and $4–3)$ and $^{13}CO(J = 2–1)$ transitions, where the $^{12}CO(J = 3–2)$ distribution is taken from

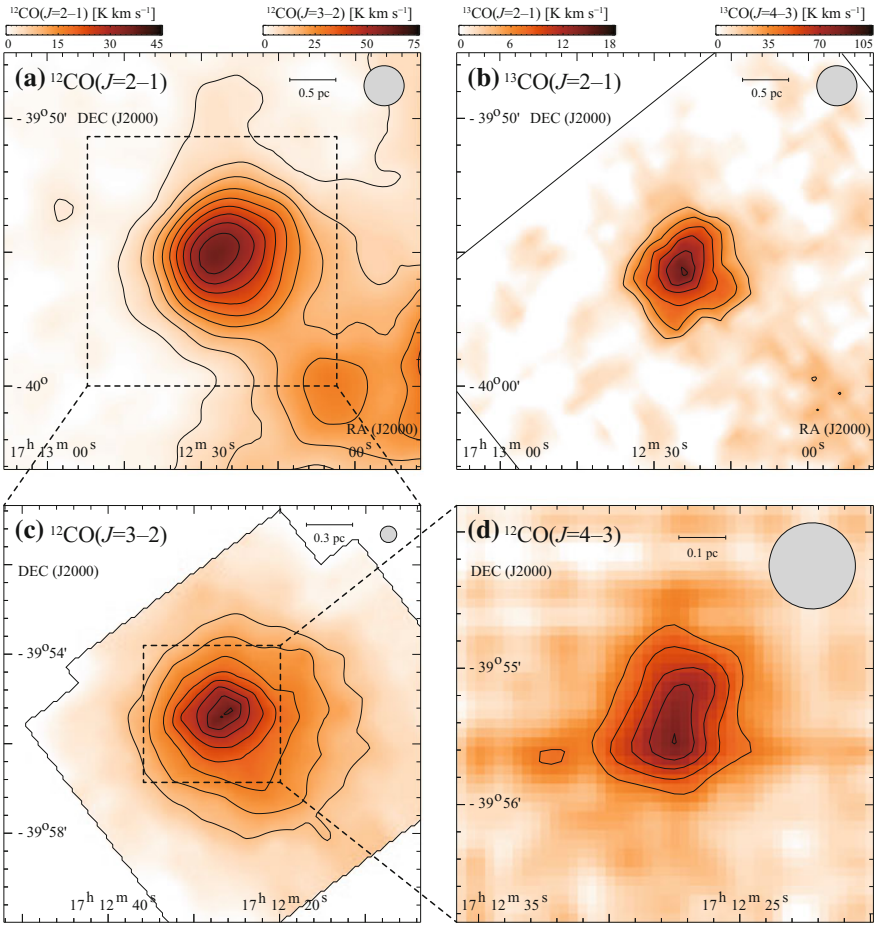

Fig. 2.10 Intensity distributions of the $^{12}CO(J = 4–3, 3–2, 2–1)$ and $^{13}CO(J = 2–1)$ transitions of clump C. The velocity range is from -30 to 7 km s^{-1} in (**d**); from -20 to -7 km s^{-1} in (**c**); from -16.6 to -7.3 km s^{-1} in (**a**); and from -16 to -8 km s^{-1} in (**b**). The CO contours are every 10.2 K km s^{-1}($\sim 3.0\sigma$) from 41.6 K km s^{-1}($\sim 12.2\sigma$) in (**d**); every 5.0 K km s^{-1} ($\sim 5.3\sigma$) from 30.2 K km s^{-1} ($\sim 31.8\sigma$) in (**c**); every 3.8 K km s^{-1} ($\sim 4\sigma$) from 2.7 K km s^{-1} ($\sim 3\sigma$) in (**a**); and every 1.8 K km s^{-1}($\sim 2.6\sigma$) from 7.28 K km s^{-1} ($\sim 10.6\sigma$) in (**d**). The lowest contours are half of the peak intensity value for each emission, except for (**a**). The open cross shows the positions of the *IRAS* point source (see Table 2.6)

(Moriguchi et al. 2005). The ^{12}CO($J = 4$–3) core is the most compact and its size increases toward the lower J transitions, suggesting a sharp intensity decrease with radius since the higher J transitions have higher critical densities for collisional excitation.

2.2.4 ^{12}CO($J = 4$–3) Broad Wings

Figure 2.11 shows that the broad ^{12}CO($J = 4$–3) wings first detected by Fukui et al. (2003) reveal a clear bipolar signature centered on *IRAS* 17089−3951 (Table 2.6) and on the peak position of the dense cloud core in clump C. This bipolarity verifies that the wings are driven by a protostar and not by the SNR shock waves. The *IRAS* source position also shows a good correlation with an extended *Spitzer* sources at 8.28 μm (from IPAC Infrared Science Archive; Fig. 2.11a). In addition to the ^{12}CO($J = 1$–0) and ^{12}CO($J = 3$–2) transitions, wings toward clump C are also seen in the current ^{12}CO($J = 2$–1) data (Moriguchi et al. 2005), although the wing intensities of these lower-J transitions are more than a few times weaker than the ^{12}CO($J = 4$–3) wings. It is not clear if clumps A and D show signs of bipolar outflow in either the ^{12}CO($J = 1$–0) and ^{12}CO($J = 3$–2) data (Moriguchi et al. 2005) or in the current ^{12}CO($J = 2$–1) data. We also find that the distribution of wing-like components is complementary to the X-ray intensity around clump C. Figure 2.12 shows two overlays of

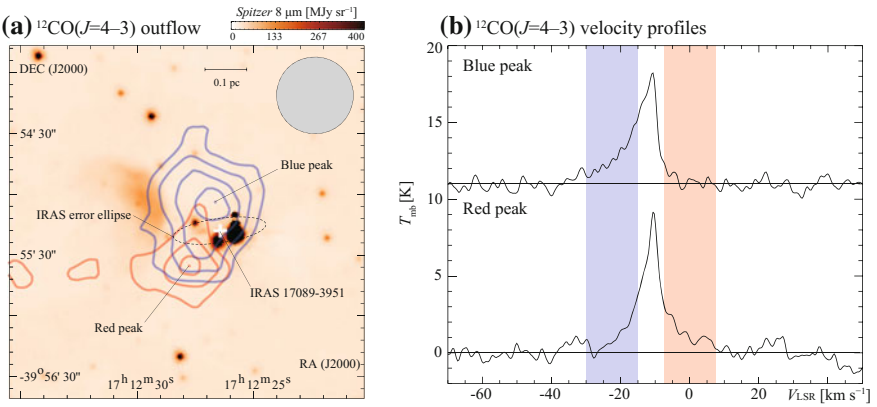

Fig. 2.11 **a** Overlay map RX J1713.7−3946 *Spitzer* 8μm image in color scale (from GRIMPS Archive) and ^{12}CO($J = 4$–3) intensity contours taken by NANTEN2. The *blue* contours are from −30 to −15 km s^{-1} and the *red* contours from −8 to 7 km s^{-1}. The lowest contour level of the *red* and *blue* contours are 9.6 K km s^{-1} (∼4σ) for each. The contour interval of the *black* contour is 10.2 K km s^{-1} (∼3σ), whereas that of the others is 4.8 K km s^{-1} (∼2σ). Open cross and enclosed *black dashed circle* show the positions of the *IRAS* point source (see Table 2.6) and the 90% confidence region, respectively. (b) ^{12}CO($J = 4$–3) spectra covering a velocity range from −70 to 50 km s^{-1}. Areas *shaded blue* and *red* correspond to the respective color contours in (**a**)

Table 2.6 Properties of *IRAS* point sources

Clump name (1)	*IRAS* point sources (2)	l (deg) (3)	b (deg) (4)	α(J2000) (^{hms}) (5)	δ(J2000) ($^{\circ\prime\prime\prime}$) (6)	semimajor $^{\prime}$ (7)	semiminor $^{\prime}$ (8)	Posang deg. (9)	F_{12} (Jy) (10)	F_{25} (Jy) (11)	F_{60} (Jy) (12)	F_{100} (Jy) (13)	L_{IRAS} ($L_{\odot}$) (14)
A	17082−3955	346.94	−0.31	17 11 41.04	−39 59 11.21	23	5	98	5.4	3.8	17.5	138	137
C	17089−3951	347.08	−0.39	17 12 26.46	−39 55 17.98	23	6	98	4.4	13.0	98.5	234	311
D	17079−3926	347.31	0.01	17 11 25.59	−39 29 53.29	39	6	98	2.0	20.0	88.6	739	562

Notes Cols. (1)–(2): Clump name (Moriguchi et al. 2005) and *IRAS* point source near the ^{12}CO($J = 3$–2) peaks. Cols. (3)–(6): Position of the *IRAS* sources. Cols. (7)–(9): Semimajor axis, semiminor axis, and position angle of the position error of the *IRAS* sources. Cols (10)–(13): Fluxes of 12, 25, 60, and 100 ¯m, respectively. Col. (14): *IRAS* luminosity estimated using the formula of Emerson (1988). Col. (18). (see Cols. (2)–(4) and (10)–(15) are Moriguchi et al. 2005 Table 3)

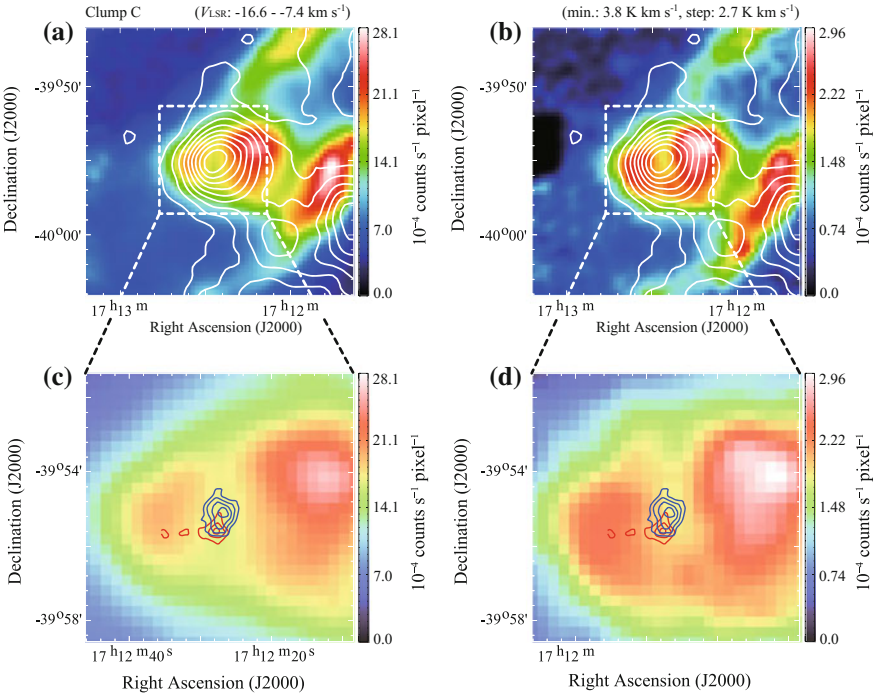

Fig. 2.12 Distribution of ^{12}CO($J = 2$–1) emission (*white contours*) superimposed on the *Suzaku* **a** 1–5 keV and **b** 5–10 keV images toward clump C. The velocity range and contour levels are the same as those in Fig. 2.5. **c** and **d** show the enlarged view of clump C overlaid with ^{12}CO($J = 4$–3) intensity contours. The contours are the same as those in Fig. 2.11a

^{12}CO($J = 4$–3) wing component and X-ray images in the 1–5 keV (Fig. 2.12a) and 5–10 keV (Fig. 2.12a) energy bands, respectively. Clump C is surrounded by bright X-ray emissions both on its east and west sides with a local minimum toward the center of the core (see also Fig. 2.5). Figure 2.12b shows a remarkable coincidence between the X-ray depression and the cloud core at a ∼0.1 pc scale. This depression is not caused by interstellar absorption, as we find a similar distribution of X-ray emissions in the higher energy band (5–10 keV) that are barely absorbed (see Appendix E). This morphology suggests that X-ray emissions are enhanced on the surface of the cloud core.

2.3 Analysis of Detailed Molecular Properties

2.3.1 LVG Analysis

We used the large velocity gradient (LVG) model of line radiation transfer to estimate density and temperature from the multi-J transitions of CO; i.e., ^{12}CO($J = 3$–2, 4–3) and ^{13}CO($J = 2$–1). We applied the LVG analysis (Goldreich and Kwan 1974; Scoville and Solomon 1974) to estimate the physical parameters of the molecular gas surrounding clumps A and C by adopting a spherically symmetric uniform model having a radial velocity gradient of dv/dr. The ^{12}CO($J = 2$–1) transition was not included in the analysis because this transition may be subject to self-absorption owing to low excitation foreground gas (e.g., Mizuno et al. 2010). We calculated level populations of ^{12}CO and ^{13}CO molecular rotational states and line intensities. The LVG model requires three independent parameters to calculate emission line intensities, i.e., kinetic temperature, density of molecular hydrogen, and $X/(dv/dr)$. $X/(dv/dr)$ is the abundance ratio between CO and H_2 divided by the velocity gradient in the cloud. Using the abundance ratio [^{12}CO]/[^{13}CO] $\sim$75 (Güsten and Philipp 2004) and [^{12}CO]/[H_2] $\sim 5\times10^{-5}$ (Blake et al. 1987), we estimated the mean velocity gradient between the peaks to be $\sim$12.5 km s^{-1} pc^{-1}. Accordingly, we adopted $X/(dv/dr) = 4.0\times10^{-6}$ (km s^{-1} pc^{-1})$^{-1}$ for ^{12}CO.

To solve for the temperatures and densities that reproduce the observed line intensity ratio, we calculated chi-square χ^2 as follows:

$$\chi^2 = \Sigma[(R_{\rm obs} - R_{\rm model})^2/\sigma] \tag{2.1}$$

where $R_{\rm obs}$ is the observed line intensity ratio between different excitation lines or isotopes, $R_{\rm model}$ is the line ratio of the LVG calculations, and σ is the standard deviation for $R_{\rm obs}$ used in the analysis. The error in the observed intensity was estimated based on the noise level of the observations and the calibration error. We assumed that an error of calibration from T_A^* to $T_{\rm MB}$ is 10% for all the line intensities. The data used were derived from the line profiles in Fig. 2.13 upper, and three ratios were estimated for a 1.5 km s^{-1} velocity interval in the three peaks, as listed in Table 2.7.

The lower panels of Fig. 2.13 show the results of fitting to the data obtained with a chi-square minimization approach to find the temperature and density solutions. Each locus of a black solid line surrounding a cross indicates the chi-square χ^2, which corresponds to the 95% confidence level of a chi-square distribution. The crosses denote the lowest point of the chi-square estimate. In addition, we are able to reject each region outside the black solid line at the 95% confidence level. Table 2.7 summarizes the results of the LVG analysis. Density and temperature are relatively well constrained in clumps A and C. The temperature of the clumps is in a range of 10–12 K, and density is somewhat higher in clump C, $\sim10^4$ cm^{-3}, than that in clump A, $\sim6\times10^3$ cm^{-3}.

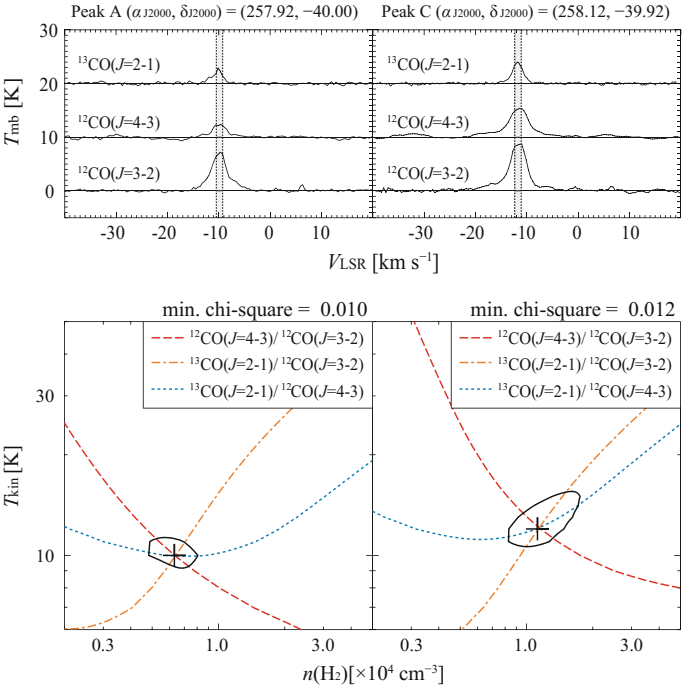

Fig. 2.13 Results of an LVG analysis for molecular clumps A and C. *Top* CO line profiles for each molecular peak are smoothed to 90″ by a Gaussian beam corresponding to the ^{13}CO($J = 2$–1) beam size. *Bottom* Results of an LVG analysis for molecular peaks as indicated by the *Top panels*. Each locus of a *black solid line* surrounding the cross indicates the chi-square χ^2 of 3.84, which corresponds to the 95% confidence level of a chi-square distribution with one degree of freedom. The crosses denote the lowest point of chi-square

Table 2.7 Results of LVG analysis at molecular clumps

Name (1)	α_{J2000} (2) (°)	δ_{J2000} (3) (°)	^{12}CO		^{13}CO	$n(H_2)$ (7) (10^4cm^{-3})	T_{kin} (K) (8)
			$J = 3$–2 (4) (K)	$J = 4$–3 (5) (K)	$J = 2$–1 (6) (K)		
A	257.92	−40.00	6.6	2.1	1.9	$0.6^{+0.2}_{-0.1}$	10^{+1}_{-1}
C	258.12	−39.92	8.5	5.2	3.4	$1.1^{+0.6}_{-0.3}$	12^{+4}_{-1}

Notes Col. (1): Clump name. Col. (2)–(3): Position of the observed point with the maximum ^{12}CO($J = 3$–2) intensity peak. Col. (4)–(6): Radiation temperature averaged to the line of sight over a velocity integral of 1.5 km s^{-1}. Col. (7): Density of molecular hydrogen. Col. (8): Kinetic temperature. The parameter $X/(dV/dR)$ =4.0 × 10^{-6} (km s^{-1} pc^{-1})$^{-1}$ is used

2.3.2 Density Distribution of Clump C

Clump C is associated with a dense cloud core with a strong intensity gradient (Fig. 2.10). The total molecular mass of the core is estimated to be 400 $M_\odot$ from the ^{12}CO(J = 1–0) integrated intensity (Moriguchi et al. 2005) for an X factor of 2.0 × 10^{20} [$W(^{12}\mathrm{CO})$/(K km s^{-1})] (Bertsch et al. 1993). We shall derive the density distribution by employing a simple power-law analysis assuming a spherical symmetry. First, we de-convolve the intensity distribution in order to correct for the beam size. We assume the relation to derive a de-convolved core radius r in each transition given by $r^2 = s^2 + r'^2$, where r, s, and r' stand for the observed radius, the beam radius, and the de-convolved radius, respectively, at a half power level of the peak intensity (Table 2.8). Then, we estimate the averaged density within r, $\overline{n(\mathrm{H_2})(< r)}$, to match

Table 2.8 Density distribution and core radius for peak C

Property	^{12}CO			^{13}CO
	J = 2–1	J = 3–2	J = 4–3	J = 2–1
Beam size (arcsec)	90	22	38	90
Core radius (pc)	0.62	0.44	0.23	0.32
Average brightness (K)	0.79	1.87	1.28	0.29
Number density (10^3cm^{-3})	0.33±0.05	1.51±0.23	3.55±0.53	1.78±0.27

Notes Cols. Number density is derived by assuming T_{kin} = 12 K and $X/(dV/dR)$ =4.0 × 10^{-6} (km s^{-1} pc^{-1})$^{-1}$. We assume that the error of density caused by calibration from T_{A}^* to T_{MB} is ±15% for all intensities

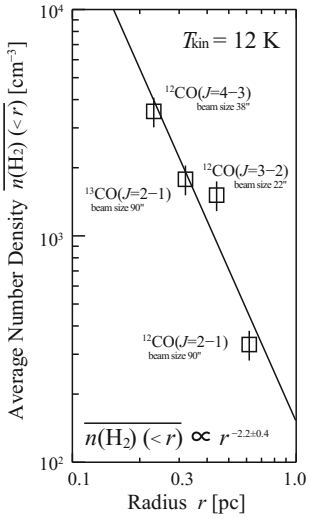

Fig. 2.14 The molecular density distribution of clump C. The calculations are conducted for T_{kin} = 12 K (see Table 2.7). The *solid line* is a regression line obtained by least squares fitting. Error bars represent only those for the radiation temperature calibration, ±15 %. See Table 2.8. for further

the observed averaged integrated intensity to the LVG estimate within the radius by assuming a kinetic temperature of 12 K and the same model parameters in Sect. 2.3.1. Considering the low luminosity of the *IRAS* source (300 $L_{\odot}$), we infer that the local temperature variation in the core is not significant and that a uniform temperature is a good approximation. The result, which is shown in Fig. 2.14, indicates that the average density distribution is well approximated by a power law, $r^{-2.2\pm0.4}$. Such a steep density gradient is consistent with a star forming cloud core (Larson 1969; Penston 1969; Lizano and Shu 1989; Onishi et al. 1999). As shown in Fig. 2.14, the line width does not vary much among the different density regimes, suggesting that the infall motion is not very large. An alternative interpretation for the density distribution will be discussed later.

2.3.3 *Physical Parameters of the Outflow*

The bipolarity of the broad CO wings in Fig. 2.11 verifies that the wings are caused by bipolar outflow driven by a protostar and is consistent with a compact dense core having a steep density gradient (Sect. 2.3.2). The physical parameters of the outflow are estimated using the method described by (Moriguchi et al. 2005, Table 2.9). The average intensities of the red component are 8.9 K and 2.0 K for the ^{12}CO(J = 2–1) and ^{12}CO(J = 4–3) transitions in a velocity range from -8 km s^{-1} to -3 km s^{-1}, respectively. The density in the line emitting wings is then estimated to be $\sim 5 \times 10^3$ cm^{-3} from the line intensity ratio, $\sim$0.23, between the ^{12}CO(J = 2–1) and ^{12}CO(J = 4–3) transitions. The beam filling factor is estimated to be as small as 5% for an assumed excitation temperature of 12 K for the rotational levels of ^{12}CO. This result is similarly obtained from the blue component, which yields a beam filling factor of $\sim$4 %. Therefore, the CO wings represent highly clumped gas, which is fairly typical for outflows. The present ^{12}CO(J = 4–3) data verify that the wings represent

Table 2.9 Outflow properties at clump C in ^{12}CO(J = 4–3)

Property	Blue component	Red component
Integrated intensity (K km s^{-1})	17.5	14.7
Size (arcmin)	0.85	0.58
Size (pc)	0.25	0.17
ΔV (km s^{-1})	15	15
$t_{\rm dyn}$ (10^4 yr)	1.6	1.1

Notes Integrated intensity is derived by summing the integrated intensities of the observed points in the area enclosed by a contour of 13.4 K within the velocity range of -30 km s^{-1} $\leq V_{\rm LSR} \leq -15$ km s^{-1} for the blue-shifted component and 11.0 K within -8 km s^{-1} $\leq V_{\rm LSR} \leq 7$ km s^{-1} for the red-shifted component, respectively. Size is defined as an effective diameter = $\sqrt{(A/\pi)} \times 2$, where A is the region enclosed by a contour of 13.4 K km s^{-1} and 11.0 K km s^{-1} for the blue-shifted and red-shifted components, respectively. ΔV is the velocity range of the wing component. The dynamical age, $t_{\rm dyn}$, is defined as $2R/\Delta V$

outflow and show that the ^{12}CO($J = 4$–3) wings are much more compact than the ^{12}CO($J = 1$–0) wings, indicating that the ^{12}CO($J = 4$–3) wings are dense outflow gases whose spatial extent is smaller than that of wings with low densities (Table 2.9, for the ^{12}CO($J = 1$–0) wings see Table 4 of Moriguchi et al. 2005). The most likely driving source of the outflow is the far infrared source *IRAS* 17089−3951. General properties for bipolar outflows are found elsewhere (e.g., Lada 1985; Fukui 1989; Fukui et al. 1993) and the outflow shown is seen to be typical in terms of size and velocity of an outflow associated with a low mass protostar.

2.4 Discussion

We present a general scenario following discussions given by Fukui et al. (2003) and Moriguchi et al. (2005). The progenitor of the supernova was a high mass star formed some Myr ago in the region that created a cavity in the ISM from its stellar wind. The local region is a star-forming region with a loose spatial association extending over a few tens of pc. Star formation in clump C may have been triggered by the progenitor of the SNR (Koo et al. 2008; Desai et al. 2010). The progenitor star caused a supernova explosion 1,600 yr ago, as recorded in a contemporary Chinese document (Wang et al. 1997), and the blast wave expanded into the cavity. The SNR is now interacting with the molecular clumps, and its interacting layer is traced by synchrotron X-rays, as supported by the high degree of spatial anti-correlation with CO clumps at a 0.1 pc scale.

We have compared the X-ray distribution with that of the CO and HI dense clumps over the entire SNR and present a schematic image of the results in Fig. 2.15. This figure indicates that the CO and dense HI clumps form an inhomogeneous shell and that the X-rays are enhanced around all the clumps. We infer that the five CO clumps C, E, I, L, and O_{SW} survived the SNR blast waves and are now embedded within the SNR, while the other twelve CO clumps and the HI clump are shock-interacting on their inner sides. As mentioned above, the ISM shell was formed over a timescale of Myr by the stellar winds of an OB star that experienced a supernova explosion 1,600 yr ago. Thus, the density in the cavity surrounded by the ISM shell is expected to be very low. The observational results also indicate that there is little dense gas left in the interior of the cavity (Figs. 2.3 and A.1). According to numerical simulations on the interaction of the ISM with the strong stellar winds from an O-type star (Weaver et al. 1977), the gas density inside the evacuated wind bubble is $\sim$0.01 cm^{-3}, which applies to the interior of the cavity.

The shock waves of the SNR first propagated in the stellar-wind cavity and then began interaction with the CO/HI clumps some 1,000 yr ago, as determined by the ratio of the shell thickness and the shock velocity, 3 pc/3000 km s^{-1}. According to MHD numerical simulations by Inoue et al. (2012), the CO/HI clumps, which have a density of $\sim 10^2$–10^3 cm^{-3}, are surrounded by an interclump gas with a density of $\sim$1 cm^{-3}, which is two orders of magnitude higher than that in the cavity. These authors showed that the shock is stalled in the dense clumps. The shock

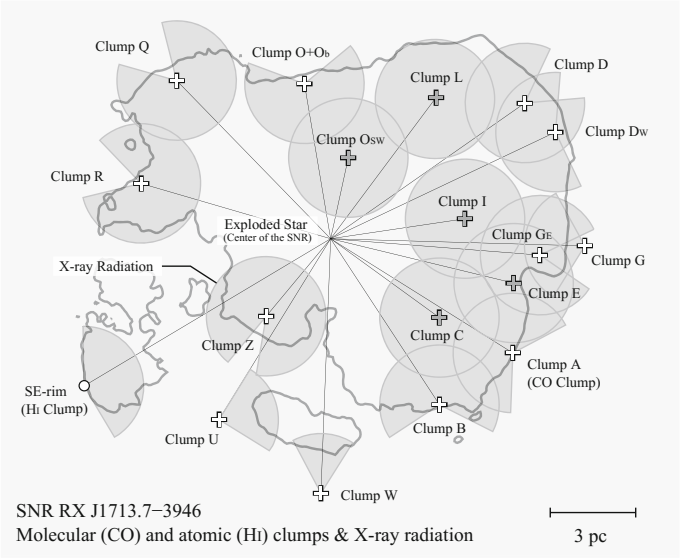

Fig. 2.15 Schematic image of the distribution of the molecular (CO) clumps (open crosses), atomic (HI) clump (*circle*) and the X-rays (shaded partial or full circles) superimposed on the *Suzaku* 1–5 keV X-ray outer boundary of the SNR (*gray* contours). The *black* open crosses (clumps C, I, E, L, and Osw) indicate the clumps fully surrounded by X-rays

velocity becomes $V_{\rm sh,clump} = V_{\rm sh,interclump}(n_{\rm interclump}/n_{\rm clump})^{0.5}$, where the interclump density $n_{\rm interclump} = 1\ {\rm cm}^{-3}$ and the clump density $n_{\rm clump} = 10^2$–$10^3\ {\rm cm}^{-3}$. The shock velocity difference between the dense CO/HI clumps and the interclump gas assumes a factor of ∼10–30. They calculated that the temperature of the shocked dense gas becomes much lower than the temperature in the post-shock diffuse gas and argued that thermal X-ray emission from the CO/HI clumps is strongly suppressed after passage of the shock (see Sect. 4.3 of Inoue et al. 2012). The interclump gas does not emit significant thermal X-rays either because the density ∼1 $\rm cm^{-3}$ is less than ∼2 $\rm cm^{-3}$, the average density inside the SNR obtained from the upper limit of the thermal X-rays (Takahashi et al. 2008). Moreover, in this case, the penetrating depth in a typical timescale of interaction of ∼1000 yr can then be estimated to be ∼0.1 pc for $n = 10^3\ {\rm cm}^{-3}$ and ∼3 pc for $n = 1\ {\rm cm}^{-3}$, respectively. Clump C has a present diameter of at least 0.6 pc and a density of $10^3\ {\rm cm}^{-3}$ (Fig. 2.14), and according to the argument above, it should not have been affected significantly by shock penetration, whereas the ambient lower density gas is significantly disturbed and accelerated over a scale length of the SNR radius. We therefore infer that clump C (and other four clumps) is able to survive against the shock wave as originally suggested by Fukui et al. (2003), whereas the lower density ambient gas is significantly disturbed and accelerated.

An important consequence of this interaction is that the large velocity difference created between the clumps and the interclump space induces turbulence, which

leads to turbulent dynamo action. The magnetic field is then amplified to as high as 1 mG, which is consistent with the field strength derived from rapid time variation of the X-ray filaments (Uchiyama et al. 2007), while an alternative is that fluctuations in field orientation may explain the rapid time variation (Helder et al. 2012). The synchrotron flux integrated over the line of sight is proportional to $B^{1.5}$ if the spectral index of electrons p is 2.0 (e.g., Rybicki and Lightman 1979). It is therefore possible to enhance the X-ray radiation around the CO and HI clumps. It is known that owing to the effect of synchrotron cooling, the power of synchrotron X-ray emission is not enhanced by magnetic field amplification if the amplification takes place in the vicinity of a forward shock where electrons are being accelerated (e.g., Nakamura et al. 2012). In the present case, as discussed by Inoue et al. (2009, 2010, 2012), the magnetic field amplification owing to the shock–cloud interaction is effective at least 0.1 pc downstream from the shock front. This indicates that the synchrotron X-rays are emitted after the acceleration process, and thus, the power of the synchrotron X-rays is enhanced by amplification. The observed power of the X-ray emission around the CO and HI clumps is 2–7 times higher than the background level inside the SNR. If the X-ray enhancement was only caused by magnetic field amplification, the magnetic field around the CO and HI clumps would be an estimated 2–4 times higher than that present elsewhere in the SNR. The averaged magnetic field around the CO and HI clumps becomes 30–60 μG if the initial field is assumed to be 15 μG (e.g., Tanaka et al. 2008). The average field strength can also be estimated from the width of synchrotron X-ray filaments as ∼100 μG (Bell 2004; Hiraga et al. 2005; Ballet 2006). Note that the dependence of the synchrotron flux on the magnetic field strength can be much more sensitive than that in the above-mentioned standard case, because the high-energy electrons that contribute the X-ray synchrotron emission can be in the cut-off regime (Bykov et al. 2008). Moreover, such enhanced magnetic field in turbulence may lead to more efficient acceleration than that in the case of diffusive shock acceleration (Lazarian and Vishniac 1999; Hoshino 2012).

Finally, we discuss the quantitative relationship between the CO/HI interacting clump mass and the X-ray enhancement. We estimated the interacting clump masses (column (9) of Table 2.8) with the shock waves as defined by the total CO/HI mass within the azimuth angle range of the X-rays with respect to the center of gravity (column (8) of Table 2.8). For the case wherein two CO clumps have small separation ($<0.^{\circ}2$) and the X-ray peak is situated between the CO clumps, we summed up the interacting clump masses and averaged the X-ray intensities (D+D_W, O+O_b+O_{SW}, G+G_E, and E+I; see also Table 2.8). In Fig. 2.16, we plot the CO/HI interacting clump mass as a function the X-ray peak intensity. Here, we approximate the mass of the SE rim to be 134 $M_\odot$ on the assumption that it has a size 0.8 pc^2 along the X-ray boundary. The result, shown in Fig. 2.16, indicates that the correlation between the interacting clump mass and the X-ray intensity is good with a correlation coefficient of ∼0.85 in double logarithm. We can conclude that the intensity is roughly proportional to the interacting mass of each CO/HI clump at a pc scale. This result suggests that the ISM distribution is crucial to producing the non-thermal X-ray distribution in young SNRs.

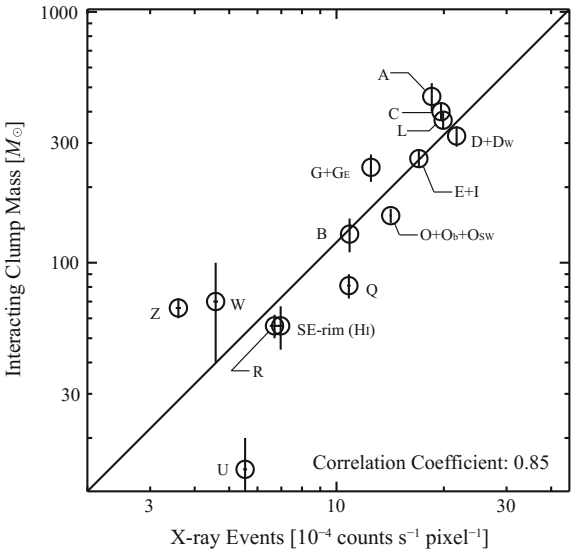

Fig. 2.16 Correlation plot between the X-ray peak intensity in the azimuthal distributions derived in Fig. 2.8 and the interacting clump mass with the shock waves, which is estimated by the CO or HI mass within the azimuth angle range of the X-rays for each clump (see for more details the text, and column (9) of Table 2.8). The linear regression by the least-squares fitting is shown by the solid line, where the correlation coefficient is ∼0.85 in double logarithm

2.5 Conclusions

We summarize the present work as follows.

1. We have shown that all the major CO and HI clumps with mass greater than 50 $M_\odot$ interacting with shock waves in RX J1713.7−3946 are associated with non-thermal X-rays. The X-rays are enhanced within ∼1 pc of the CO and HI peaks, whereas at smaller scales down to 0.1 pc, the CO peaks tend to be anti-correlated with X-ray intensity, which is decreased around the CO and HI clumps. We have shown good correlation between the CO/HI clump mass interacting with the shock waves and the X-ray intensity.
2. Sub-millimeter results indicate that the core of clump C has a strong density gradient consistent with an average density distribution of $r^{-2.2\pm0.4}$, where r is the radius from the center of the core. The density and temperature, averaged over $90''$ (= 0.2 pc), are 0.8–1.7 × 10^4 cm^{-3} and 11–16 K, respectively, as derived from the LVG analysis. Clump C is also associated with a bipolar outflow as evidenced by the ^{12}CO(J = 4–3) broad wings of at least 30 km s^{-1} velocity extent. Along with the far infrared spectrum, these identify the region as a site of recent low-mass star formation within Myr. This verifies that the broad wings are not produced by the shock acceleration driven by the SNR, as suggested before by Fukui et al. (2003). Clump A has density and temperature of 5–8 × 10^3 cm^{-3} and 9–11 K, respectively, somewhat lower than those of clump C. The *IRAS* sources in clump A and D are also likely protostars, as noted by Moriguchi et al. (2005), because of the high density of these peaks.

3. The present findings in (1) are compared with numerical simulations of MHD in a realistic highly inhomogeneous density distribution by Inoue et al. (2009, 2012). These simulations indicate that the magnetic field is amplified around dense CO/HI clumps as a result of enhanced turbulence induced by the shock–cloud interaction. We interpret that magnetic fields amplified by this interaction enhance the X-ray intensity, which is proportional to the 1.5-th power of the magnetic field strength. Such enhanced magnetic fields may also lead to efficient acceleration additional to the DSA. More comparative study of the distribution of X-rays and the ISM will allow us to develop deeper insight into the origin of X-ray distributions.

References

J. Ballet, Adv. Space Res. **37**, 1902 (2006)
A.R. Bell, Mon. Not. R. Astron. Soc. **353**, 550 (2004)
D.L. Bertsch, T.M. Dame, C.E. Fichtel, S.D. Hunter, P. Sreekumar, J.G. Stacy et al., Astrophys. J. **416**, 587 (1993)
G.A. Blake, E.C. Sutton, C.R. Masson, T.G. Phillips, Astrophys. J. **315**, 621 (1987)
M. Burgay, N. Rea, G.L. Israel, A. Possenti, L. Burderi, T. di Salvo et al., Mon. Not. R. Astron. Soc. **372**, 410 (2006)
A.M. Bykov, Y.A. Uvarov, D.C. Ellison, Astrophys. J. Lett. **689**, L133 (2008)
R.M. Cutri, M.F. Skrutskie, S. van Dyk, C.A. Beichman, J.M. Carpenter, T. Chester et al., VizieR Online Data Catalog **2246** (2003)
L.K. Denoyer, Astrophys. J. Lett. **232**, L165 (1979)
K.M. Desai, Y.-H. Chu, R.A. Gruendl, W. Dluger, M. Katz, T. Wong et al., Astron. J. **140**, 584 (2010)
R.P. Eatough, M. Kramer, A.G. Lyne, M.J. Keith, Mon. Not. R. Astron. Soc. **431**, 292 (2013)
J.P. Emerson, NATO ASIC Proceedings 241: Formation and Evolution of Low Mass Stars, vol. 193 (1988)
Y. Fukui, T. Iwata, A. Mizuno, J. Bally, A.P. Lane, Protostars and Planets **III**, 603 (1993)
Y. Fukui, Eur. South. Obs. Conf. Workshop Proc. **33**, 95 (1989)
Y. Fukui, Y. Moriguchi, K. Tamura, H. Yamamoto, Y. Tawara, N. Mizuno et al., Publ. Astron. Soc. Jpn. **55**, L61 (2003)
Fukui,Y. in, *AIP Conference Proceedings, Proceedings of 4th International Meeting on High-Energy Gamma-Ray Astronomy*, ed. F.A. Aharonian, W. Hofmann, F. Rieger, Vol. 1085, p. 104 (Melville, NY: AIP, 2008)
Y. Fukui, H. Sano, J. Sato, K. Torii, H. Horachi, T. Hayakawa et al., Astrophys. J. **746**, 82 (2012)
R. Güsten, S.D. Philipp, The Dense Interstellar Medium in Galaxies, vol. 253 (2004)
P. Goldreich, J. Kwan, Astrophy. J. **189**, 441 (1974)
M. Gottwald, A.N. Parmar, A.P. Reynolds, N.E. White, A. Peacock, B.G. Taylor, Astron. Astrophys. Suppl. **109**, 9 (1995)
S. Guillot, R.E. Rutledge, E.F. Brown, G.G. Pavlov, V.E. Zavlin, Astrophys. J. **699**, 1418 (2009)
E.A. Helder, J. Vink, A.M. Bykov, Y. Ohira, J.C. Raymond, R. Terrier, Space Sci. Rev. **173**, 369 (2012)
J.S. Hiraga, Y. Uchiyama, T. Takahashi, F.A. Aharonian, Astron. Astrophys. **431**, 953 (2005)
M. Hoshino, Phys. Rev. Lett. **108**, 135003 (2012)
T. Inoue, R. Yamazaki, S.-I. Inutsuka, Astrophys. J. **695**, 825 (2009)
T. Inoue, R. Yamazaki, S.-I. Inutsuka, Astrophys. J. Lett. **723**, L108 (2010)
T. Inoue, R. Yamazaki, S.-I. Inutsuka, Y. Fukui, Astrophys. J. **744**, 71 (2012)

Y. Ishisaki, Y. Maeda, R. Fujimoto, M. Ozaki, K. Ebisawa, T. Takahashi et al., Publ. Astron. Soc. Jpn. **59**, 113 (2007)
B.-C. Koo, C.F. McKee, J.-J. Lee, H.-G. Lee, J.-E. Lee, D.-S. Moon et al., Astrophys. J. Lett. **673**, L147 (2008)
K. Koyama, K. Kinugasa, K. Matsuzaki, M. Nishiuchi, M. Sugizaki, K. Torii et al., Publ. Astron. Soc. Jpn. **49**, L7 (1997)
K. Koyama, H. Tsunemi, T. Dotani, M.W. Bautz, K. Hayashida, T.G. Tsuru et al., Publ. Astron. Soc. Jpn. **59**, 23 (2007)
C.A. Kulesa, A.L. Hungerford, C.K. Walker, X. Zhang, A.P. Lane, Astrophys. J. **625**, 194 (2005)
C.J. Lada, Ann. Rev. Astron. Astrophys. **23**, 267 (1985)
H. Landt, H.E. Bignall, Mon. Not. R. Astron. Soc. **391**, 967 (2008)
R.B. Larson, Mon. Not. R. Astron. Soc. **145**, 271 (1969)
A. Lazarian, E.T. Vishniac, Astrophys. J. **517**, 700 (1999)
J.S. Lazendic, P.O. Slane, B.M. Gaensler, P.P. Plucinsky, J.P. Hughes, D.K. Galloway et al., Astrophys. J. Lett. **593**, L27 (2003)
D. Lin, N.A. Webb, D. Barret, Astrophys. J. **756**, 27 (2012)
S. Lizano, F.H. Shu, Astrophys. J. **342**, 834 (1989)
F.J. Lu, T.P. Li, X.J. Sun, M. Wu, C.G. Page, Astron. Astrophys. Suppl. **115**, 395 (1996)
N.M. McClure-Griffiths, J.M. Dickey, B.M. Gaensler, A.J. Green, M. Haverkorn, S. Strasser, Astrophys. J. **158**, 178 (2005)
Y. Mizuno, A. Kawamura, T. Onishi, T. Minamidani, E. Muller, H. Yamamoto et al., Publ. Astron. Soc. Jpn. **62**, 51 (2010)
Y. Moriguchi, K. Tamura, Y. Tawara, H. Sasago, K. Yamaoka, T. Onishi et al., Astrophys. J. **631**, 947 (2005)
H. Nakajima, H. Yamaguchi, H. Matsumoto, T.G. Tsuru, K. Koyama, H. Tsunemi et al., Publ. Astron. Soc. Jpn. **60**, 1 (2008)
R. Nakamura, A. Bamba, T. Dotani, M. Ishida, R. Yamazaki, K. Kohri, Astrophys. J. **746**, 134 (2012)
T. Onishi, A. Mizuno, Y. Fukui, Publ. Astron. Soc. Jpn. **51**, 257 (1999)
M.V. Penston, Mon. Not. R. Astron. Soc. **145**, 457 (1969)
E. Pfeffermann, B. Aschenbach, in, *Proceedings of Roentgenstrahlung from the Universe*, ed. H.U. Zimmermann, J.H. Trümper, H. Yorke, vol. 267 (1996)
J.L. Pineda, N. Mizuno, J. Stutzki, M. Cubick, M. Aravena, F. Bensch et al., Astron. Astrophys. **482**, 197 (2008)
A.P. Reynolds, A.N. Parmar, P.J. Hakala, A.M.T. Pollock, O.R. Williams, A. Peacock et al., Astron. Astrophys. Suppl. **134**, 287 (1999)
G.B. Rybicki, A.P. Lightman, *Radiative Processes in Astrophysics* (Wiley-Interscience, New York, 1979)
N. Schneider, J. Stutzki, G. Winnewisser, D. Block, Astron. Astrophys. **335**, 1049 (1998)
N.Z. Scoville, P.M. Solomon, Astrophys. J. Lett. **187**, L67 (1974)
P.J. Serlemitsos, Y. Soong, K.-W. Chan, T. Okajima, J.P. Lehan, Y. Maeda et al., Publ. Astron. Soc. Jpn. **59**, 9 (2007)
P. Slane, B.M. Gaensler, T.M. Dame, J.P. Hughes, P.P. Plucinsky, A. Green, Astrophys. J. **525**, 357 (1999)
P. Slane, J.P. Hughes, R.J. Edgar, P.P. Plucinsky, E. Miyata, H. Tsunemi et al., Astrophys. J. **548**, 814 (2001)
T. Takahashi, K. Abe, M. Endo, Y. Endo, Y. Ezoe, Y. Fukazawa et al., Publ. Astron. Soc. Jpn. **59**, 35 (2007)
T. Takahashi, T. Tanaka, Y. Uchiyama, J.S. Hiraga, K. Nakazawa, S. Watanabe et al., Publ. Astron. Soc. Jpn. **60**, 131 (2008)
T. Tanaka, Y. Uchiyama, F.A. Aharonian, T. Takahashi, A. Bamba, J.S. Hiraga et al., Astrophys. J. **685**, 988 (2008)
W.W. Tian, Z. Li, D.A. Leahy, J. Yang, X.J. Yang, R. Yamazaki et al., Astrophys. J. **712**, 790 (2010)

Y. Uchiyama, T. Takahashi, F.A. Aharonian, Publ. Astron. Soc. Jpn. **54**, L73 (2002)
Y. Uchiyama, F.A. Aharonian, T. Tanaka, T. Takahashi, Y. Maeda, Nature **449**, 576 (2007)
H. Uchiyama, M. Ozawa, H. Matsumoto, T.G. Tsuru, K. Koyama, M. Kimura et al., Publ. Astron. Soc. Jpn. **61**, 9 (2009)
M. van den Berg, K. Penner, J. Hong, J.E. Grindlay, P. Zhao, S. Laycock et al., Astrophys. J. **748**, 31 (2012)
K.A. van der Hucht, New A Rev. **45**, 135 (2001)
W. Voges, B. Aschenbach, T. Boller, H. Bräuninger, U. Briel, W. Burkert et al., Astron. Astrophys. **349**, 389 (1999)
Z.R. Wang, Q.-Y. Qu, Y. Chen, Astron. Astrophys. **318**, L59 (1997)
R. Weaver, R. McCray, J. Castor, P. Shapiro, R. Moore, Astrophys. J. **218**, 377 (1977)
H.A. Wootten, Astrophys. J. **216**, 440 (1977)
A. Wootten, Astrophys. J. **245**, 105 (1981)
V.N. Zirakashvili, F. Aharonian, Astron. Astrophys. **465**, 695 (2007)
V.N. Zirakashvili, F.A. Aharonian, Astrophys. J. **708**, 965 (2010)

http://www.springer.com/978-4-431-55635-0

Shock-Cloud Interaction in RX J1713.7−3946
Evidence for Cosmic-Ray Acceleration in the Young VHE γ-ray Supernova Remnant

Sano, H.

2017, XIII, 134 p. 60 illus., 53 illus. in color., Hardcover
ISBN: 978-4-431-55635-0